

**Automatic LbL-LPE Spin-Coating Strategy for the Fabrication of Highly Oriented
Mixed-Linker MOF Thin Films for Orientation-Dependent Applications**

Eleonora Afanasenko,¹ Benedetta Marmiroli,² Behnaz Abbasgholi-NA,³ Barbara Sartori²,
Giovanni Birarda,⁴ Chiaramaria Stani,⁴ Matjaž Finšgar,⁵ Peter E. Hartmann,⁶ Mark Bieber,⁷
Emma Walitsch,⁷ Rolf Breinbauer,⁷ Simone Dal Zilio,³ Sumea Klokic^{2*} and Heinz Amenitsch^{2*}

1 CERIC-ERIC, Trieste, Italy

2 Institute of Inorganic Chemistry, University of Technology, Graz, Austria

3 Istituto Officina dei Materiali - CNR-IOM, Trieste, Italy

4 Elettra Sincrotrone Trieste, Trieste, Italy

5 Faculty of chemistry and chemical engineering, University of Maribor, Slovenia

6 Institute of Physical and Theoretical Chemistry, University of Graz, Austria

7 Institute of Organic Chemistry, University of Technology, Graz, Austria

Abstract

Control over crystallographic orientation in metal-organic framework (MOF) thin films is essential, as many of their functional properties critically depend on exact alignment along a defined crystallographic direction. Spin-assisted layer-by-layer liquid-phase epitaxy (LbL-LPE) offers significant advantages over conventional synthesis approaches, including reduced chemical consumption, shorter processing times, and operation under ambient conditions. In this work, this LbL-LPE spin-coating is established as a robust, high-throughput fabrication protocol suitable for application-ready materials. The flexible pillar-layered framework $\text{Zn}_2\text{BDC}_2\text{DABCO}$ serves as a proof-of-concept framework for the development of an automated spin-assisted LbL-LPE workflow enabling reproducible fabrication of homogeneous and highly oriented MOF thin films with integrated monitoring of critical processing steps. The protocol incorporates correlative characterization combining grazing-incidence wide-angle X-ray scattering (GIWAXS), infrared and UV–Vis spectroscopy, scanning electron microscopy (SEM), and time-of-flight secondary ion mass spectrometry (ToF-SIMS) to ensure control over surface chemistry, reactant delivery, and film growth. Determination of the degree of orientation and the Hermans orientation parameters provides a key quality metrics for assessing crystal alignment and reproducibility. The automated experimental workflow significantly accelerates the fabrication of thin films whose properties depend on crystal orientation, providing processing optimizations and control that can be readily extended to increasingly complex MOF architectures.

1. Introduction

The fabrication of oriented crystalline materials has become increasingly important for the development of films whose properties depend on alignment along a specific crystallographic axis.^[1,2] A prominent example is given by metal-organic frameworks (MOFs), which consist of ordered networks of metal nodes and organic linkers that offer exceptional compositional tunability, high surface area and porosity, rendering them attractive for gas storage, sensing, and separation.^[3-6] For many of these applications, exact control over crystallographic orientation is essential because many MOF properties, including gas permeability,^[7,8] optical properties,^[9,10] or photo-induced structural dynamics,^[11,12] exhibit directional dependence arising from lattice anisotropy. Oriented MOF films display optical birefringence and anisotropic fluorescence when crystallites are aligned,^[9,13] enhanced directional gas permeation in membranes with preferential pore-channel alignment,^[14] and orientation-dependent structural dynamics in stimuli-responsive frameworks.^[15,16] These examples highlight that crystallographic alignment can strongly enhance or suppress functional performance, making oriented MOF films critical for maximizing directional responses and enabling reliable integration into devices such as sensors, switches, and electronic components, where uniformity and reproducibility are required.^[17-21]

To date, several strategies have been developed to grow oriented MOFs on surfaces, including liquid-phase epitaxy (LPE),^[22,23] layer-by-layer assembly (LbL),^[24] substrate-seeded heteroepitaxy (SSH),^[9,25,26] vapor-assisted conversion (VAC),^[27] and various external-field-assisted approaches, as comprehensively reviewed elsewhere.^[28-30] Each of these methods offers distinct advantages as well as inherent limitations, only some of them enable controllable or even tunable crystallographic orientation. Within this context, layer-by-layer liquid-phase epitaxy (LbL-LPE) is attractive for its low chemical consumption and enhanced environmental sustainability. Among LbL-LPE approaches, the spin-assisted method introduced by Chernikova et al.^[31] particularly stands out due to its reduced solvent use, minimized cross-

contamination due to direct deposition of reactants onto substrate, avoiding vessels with reactant solutions, exact thickness control through the number of deposition cycles, and shorter fabrication times with respect to other LPE methods. Despite these strengths, spin-assisted LbL-LPE has not yet been translated into a robust high-throughput workflow that provides reproducible orientation control, and enables real-time monitoring and adjustment of critical process parameters, which is crucial for its transferability across different MOF chemistries. [25,32] To date, only a limited number of studies have explored LbL spin-coating methods for MOF film fabrication, primarily for MOFs with a single ligand type such as ZIF-8, HKUST-1, and $\text{Cu}_2(\text{bdc})_2 \cdot x\text{H}_2\text{O}$, SURMOF-2-type^[33] or bimetallic MOF films.^[34] In contrast, mixed-ligand or pillar-layered frameworks, highly relevant in the design of structurally adaptive materials, remain largely unexplored.^[5,7] In such systems, orientation control is particularly valuable because anisotropic pore contraction,^[9] light-responsive behaviour,^[5,8] or guest-induced deformations^[6] can propagate differently along distinct lattice directions and eventually affecting the final response characteristics and functionality of the film.^[7]

Here, we address these challenges by developing an automated, spin-assisted LbL-LPE protocol with integrated monitoring of all critical steps to obtain reproducible, homogeneous, and highly oriented MOF films (**Figure 1**). The workflow incorporates contact-angle analysis to verify self-assembled monolayer (SAM) functionalization, UV-visible spectroscopy to adjust reactant concentrations. The reliability of the protocol is assessed by a correlative characterization strategy combining grazing-incidence wide-angle X-ray scattering (GIWAXS), grazing-incidence reflectance (GIR) spectromicroscopy, scanning electron microscopy (SEM) and time of flight secondary-ion mass spectrometry (ToF-SIMS). As a proof-of-concept system, we selected the flexible pillar-layered framework $\text{Zn}_2\text{BDC}_2\text{DABCO}$ (BDC = terephthalate, DABCO = 1,4-diazabicyclo[2.2.2]octane), due to its structural flexibility and its demonstrated ability to enable exceptional photoresponsive behavior and efficient CO_2 uptake, as previously shown in SSH-grown oriented films by some of the authors present in this study. [3,11,35]

By systematically varying the Zn:BDC:DABCO ratio, we establish a regime conducive to the formation of highly oriented films, with the (001) reflection aligned parallel to the substrate surface. Deviations from this ratio are associated with the emergence of partial (100) domains visible in the GIWAXS patterns and corroborated by SEM, demonstrating the sensitivity of pillar-layered frameworks to reactant stoichiometry and the importance of controlled reaction conditions. Employing both the commercially available SAM 16-mercaptohexadecanoic acid (MHDA) and the synthetically accessible pyridine-terminated (4-(4-pyridyl)phenyl)methanethiol (PP1), Zn_2BDC_2DABCO films can be prepared with high homogeneity and a pronounced degree of crystallographic orientation relative to the substrate. The LbL-LPE fabrication process requires only seconds of active deposition time per cycle, and, due to low reagent consumption and room-temperature conditions, is readily transferable to other MOF systems with comparable coordination chemistry. In addition, a modular software package that automates and logs each fabrication step was developed, which enables exact control and straightforward implementation of the spin-coating LbL-LPE process.

This workflow establishes a reproducible and scalable route toward oriented MOF thin films and provides a general platform for extending automated LbL-LPE to more complex or structurally adaptive frameworks. By implementing an integrated, software-controlled spin-assisted LbL-LPE protocol, we achieve robust fabrication of homogeneous and highly oriented films, including complex pillar-layered architectures. This workflow lays the foundation for high-throughput, device-compatible fabrication of oriented MOF films opening opportunities for orientation-dependent applications such as directional gas separation membranes, anisotropic sensors, optoelectronic devices, and stimuli-responsive actuators.

2. Synthesis of the $\text{Zn}_2(\text{BDC})_2\text{DABCO}$ *via* LBL-LPE spin-coating

2.1 LPE spin-coating protocol

The automated LPE spin-coating protocol comprises three sequential steps, schematically outlined in **Figure 1**, each followed by a quality control check to ensure reproducible $\text{Zn}_2\text{BDC}_2\text{DABCO}$ thin film growth with controlled orientation, thickness, and uniformity.

The deposition process was carried out on gold substrates that were pre-functionalized with self-assembled monolayers (SAMs), which served as the starting point for film growth. The spin-coating step is fully automated using a motorized arm equipped with three PTFE tubes, each connected to a separate syringe that holds the working solutions of either zinc acetate (M), mixed-linker BDC–DABCO (L), and solvent ethanol as the washing agent (S). The syringes are mounted on syringe pumps, which deliver the solutions dropwise through the tubing onto the substrate (**Figure S1 a,b**).

A single deposition cycle follows the sequence S-M-S-L-S and defines one growth cycle (**Figure S1 c**). All deposition steps, positioning of the tubes, addition of solutions, control of syringe pumps, and dispensed volumes, are fully automated and coordinated by an in-house developed software written in LabView (National Instruments, USA). Prior to each deposition step, the corresponding PTFE tube is automatically positioned at the substrate center. At the conclusion of the deposition cycles, the films are immediately removed from the spin-coater and gently dried under nitrogen flow. Herein, $\text{Zn}_2\text{BDC}_2\text{DABCO}$ thin films were prepared using either 60 or 120 deposition cycles.

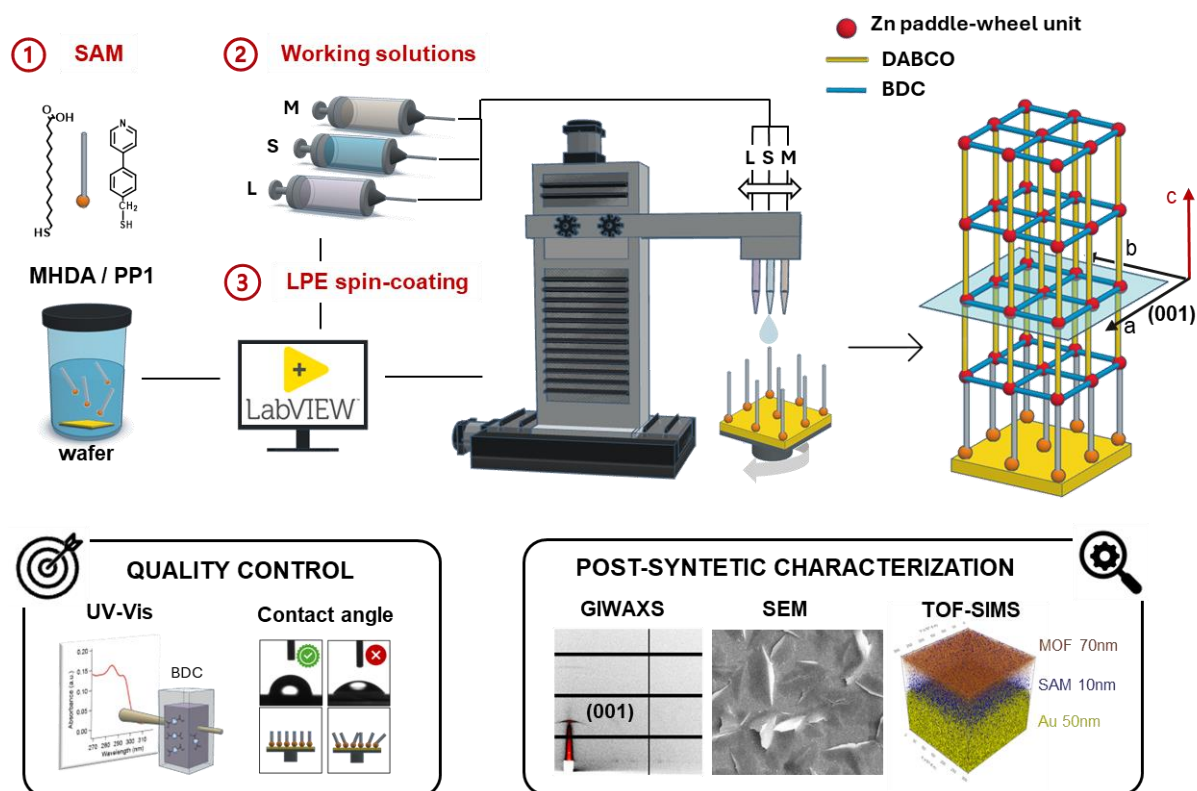


Figure 1. Schematic representation of the spin-assisted LbL-LPE protocol. The workflow comprises three main processing steps, each accompanied by a corresponding quality-control or characterization stage: (1) Functionalization of Au-wafers with MHDA or PP1 SAMs, with surface quality checked by contact angle measurements; (2) Preparation of precursor solutions with concentrations measured by UV-visible spectroscopy; (3) Fully automated layer-by-layer deposition controlled *via* LabVIEW software, resulting in the formation of a (001)-oriented MOF thin film, followed by structural characterization.

3. Results and discussion

3.1. Optimization of the LbL-LPE workflow

To guarantee the reproducibility and efficacy of the established fabrication protocol, careful optimization of all parameters was performed, and strict monitoring of the critical steps, such as concentration of the solutions and SAM quality, termed hereinafter as quality control, was implemented after each process step (Figure 1, see 1-3). The first step, namely functionalization

of the Au-wafers, was performed following well-established literature procedures.^[5] Substrates were immersed for 24 h in a 0.02 mM solution of MHDA containing acetic acid, or in a solution of PP1. Both SAM-forming molecules are known to exhibit high chemical stability over a broad range of experimental conditions and are therefore widely used as anchoring layers in the synthesis of surface-mounted MOFs.^[36–38] However, prolonged storage of the functionalized wafers is known to induce surface disorder, which can adversely affect subsequent MOF growth.^[39,40] In this study, degradation of the SAM layer after storage was experimentally confirmed by contact angle measurements (**Figure S2 a**). Well-ordered MHDA monolayers exhibit pronounced hydrophilicity due to their terminal –COOH groups, reflected by contact angles (α) of approximately $\alpha = 30^\circ$, while defective or disordered SAMs display increased hydrophobicity with contact angles around $\alpha = 50^\circ$. A comparable effect was observed for PP1 SAMs ($\alpha = 35^\circ$ for the well-ordered after loss of order $\alpha = 53^\circ$), which combine a hydrophilic pyridine moiety with a hydrophobic aromatic backbone. According to previous reports,^[39–43] SAM degradation has been attributed to UV-induced oxidation of the sulphur head groups and is further promoted by both poor gold substrate quality or functionalization procedures. Building on this knowledge, herein, only freshly SAM-functionalized substrates not older than 48 hours were employed for the LPE spin-coating process to overcome potential surface disorder and improve full reproducibility of the resulting MOF thin films, crucial for the reliable comparison of their crystallographic orientation and related properties (*vide infra*).

During the second step in the fabrication process (Figure 1, step 2) involving the preparation of the working solutions, the ethanolic H₂BDC solution is first analyzed by UV-Vis spectroscopy to verify its concentration. DABCO is added only afterward, as the overlapping absorbance bands of both linkers preclude reliable differentiation in a single solution (Figure S2 b). Working solutions were typically used for no more than three days to prevent ligand crystallization or the formation of Zn(OH)₂^[44,45]. It is important to note that one of the key factors influencing the quality of films produced by the LPE spin-coating process is the careful

optimization of both the linker-to-linker and metal-to-linker ratios, which will be discussed in detail in Section 3.2. The optimal concentrations for reproducible fabrication of oriented and uniform MOF films were determined to be Zn:BDC:DABCO = 0.1 mM : 0.1 mM : 0.3 mM. Even small deviations from these concentrations provoke significant differences in the resulting film, making exact control over solution preparation critically important.

During the automatic deposition step (Figure 1, step 3), 33 μL of each solution, determined empirically, is dispensed sequentially onto the functionalized substrate at a pumping rate of 0.2 $\mu\text{L min}^{-1}$ while the substrate is continuously rotating at 550 rpm. The tube height relative to the substrate was fixed at 10 mm to control droplet impact and prevent coverage issues arising from the surface tension effect. It was empirically determined that higher spinning speeds (800–1000 rpm) lead to undesired drying during the spinning process, resulting in the absence of film growth. In contrast, at lower speeds (450–500 rpm), the rotation becomes unstable, compromising the homogeneity of film coverage. At the optimal speed of 550 rpm, film growth through self-assembly in the solution that requires exact stoichiometric control (see Chapter 3.2). Between each injection, the sample is washed with ethanol to remove excess reagents and maintain uniform deposition. At the end of the deposition process, the film is carefully removed from the spin-coater and dried under a gentle nitrogen stream, as drying while spinning compromises crystallinity, which is observed in the GIWAXS patterns (Figure S2 c), even though the chemical fingerprint remains unchanged, as evidenced by IR (Figure S2 c).

Film homogeneity at a molar ratio of BDC:DABCO = 1:3 was assessed using grazing-angle infrared (GAIR) spectromicroscopy, which provides spatially resolved chemical analysis across large substrate areas on thin films. Under these controlled fabrication conditions, uniform chemical composition is achieved across the entire substrate, including the wafer edges. This is confirmed by raster scanning the sample and comparing 400 spectra distributed across the entire sample area (**Figure S3 a**). Under the selected spinning speed and stoichiometric conditions, complete wafer coverage was achieved without inhomogeneities on the wafer edges, commonly

associated with spin-coated films (Figure S3 a,b). The reproducibility of the automated LbL-LPE fabrication was verified by measuring the IR spectra of independently synthesized samples (**Figure S4**) and by quantifying the degree of orientation and Hermans orientation parameter, as described in Section 3.3. Further post-synthetic characterization, along with an analysis of how variations in reagents' molar ratios affect sample morphology and crystallinity, is presented in the following section.

3.2. Structural and morphological characterization of LbL-LPE spin-coated films

Conventional approaches to MOF synthesis often employ elevated temperatures, extended reaction times, or organic solvents to enhance reaction kinetics, however, such strategies are incompatible with the present spin-coating methodology. Instead, this constraint was transformed into an advantage, enabling clean, efficient, and highly reproducible thin-film formation with minimal reagent consumption. Considering fundamental principles of reactant stoichiometry and the roles of limiting and excess reagents in MOF assembly,^[46–49] we aimed to establish a stoichiometric growth window that enables the reproducible fabrication of preferentially oriented, uniform films under ambient conditions. To achieve this goal experimentally, films obtained by 60 and 120 deposition cycles grown using BDC:DABCO molar ratios of 1:1, 1:2, 1:3, 1:4, and 1:5 were characterized by SEM and GIWAXS. Their chemical composition was analyzed by IR spectromicroscopy. The assignment of the IR peaks (Table S3) was performed based on a DFT-calculated spectrum with computational details provided in the Supplementary Information in Chapter 5, including **Figures S5–S11** and **Tables S1–S3**.^[26,50–52]

GIWAXS measurements reveal a pronounced dependence of the crystallographic orientation of Zn₂BDC₂DABCO thin films on the linker-to-linker ratio (**Figure 2 a**). At a BDC:DABCO ratio of 1:1, framework formation is strongly hindered, as evidenced by weak and diffuse reflections for PP1-functionalized substrates and the absence of detectable diffraction for MHDA-functionalized samples. The IR spectrum of this composition exhibits a peak at 1585

cm^{-1} , indicative of Zn coordination to the BDC ligands, while the absence of the C–N–C bending vibration at 1479 cm^{-1} reveals insufficient DABCO amount (Figure 2 b). GIWAXS results show that increasing the relative DABCO content enhances framework formation, reflected by a sharp increase in the intensity of the (001) reflection. For films grown after 60 deposition cycles with BDC:DABCO ratios exceeding 1:1, a strong diffraction peak corresponding to the (001) lattice plane is observed, indicating preferential alignment of the MOF lattice parallel to the substrate surface (out-of-plane orientation). This pronounced out-of-plane alignment occurs irrespective of the SAM functionalization, demonstrating that stoichiometric control dominates over surface functionalization in determining lattice orientation along the surface normal (Figure 2 a). Comparison with the powder diffraction pattern (**Figure S12**) confirms that the resulting film adopts the tetragonal P4/mmm structure.^[53] Further analysis *via* grazing-incidence infrared (GIR) spectromicroscopy (Figure 2 b) shows the characteristic asymmetric and symmetric carboxylate stretching vibrations at 1624 and 1402 cm^{-1} , respectively, confirming coordination of the BDC linker.

Films grown at BDC:DABCO ratios of 1:2 and 1:3 display the highest degree of out-of-plane orientation and film homogeneity, with the 1:3 ratio approaching a nearly single-crystal-like alignment, as evidenced by intensity focused into discrete spots (Figure 2 a). When the DABCO content exceeds the 1:3 ratio, namely, at ratios of 1:4 and 1:5, the diffraction intensity spreads over a wider azimuthal angle (χ), reflecting a reduction of crystal lattice alignment (Figure 2 a). Simultaneously, the overall intensity of the (001) reflection decreases, indicating that excessive DABCO again hampers the formation of well-ordered films. This finding is corroborated by IR spectroscopic results, which show a peak at 1294 cm^{-1} corresponding to unreacted DABCO, appearing only for the 1:5 ratio. For all films with ratios above 1:1, the (001) reflection remains the most intense in the out-of-plane direction, indicating that the lattice alignment relative to the substrate is preserved, with the c-axis consistently oriented perpendicular to the surface. Notably, this excellent out-of-plane crystallographic alignment does not translate to the in-plane

direction, where no preferential azimuthal orientation is observed, indicating that crystallites are isotropically distributed along the substrate plane. This combination of strong out-of-plane texture and in-plane isotropy results in a textured film rather than a fully epitaxial layer.

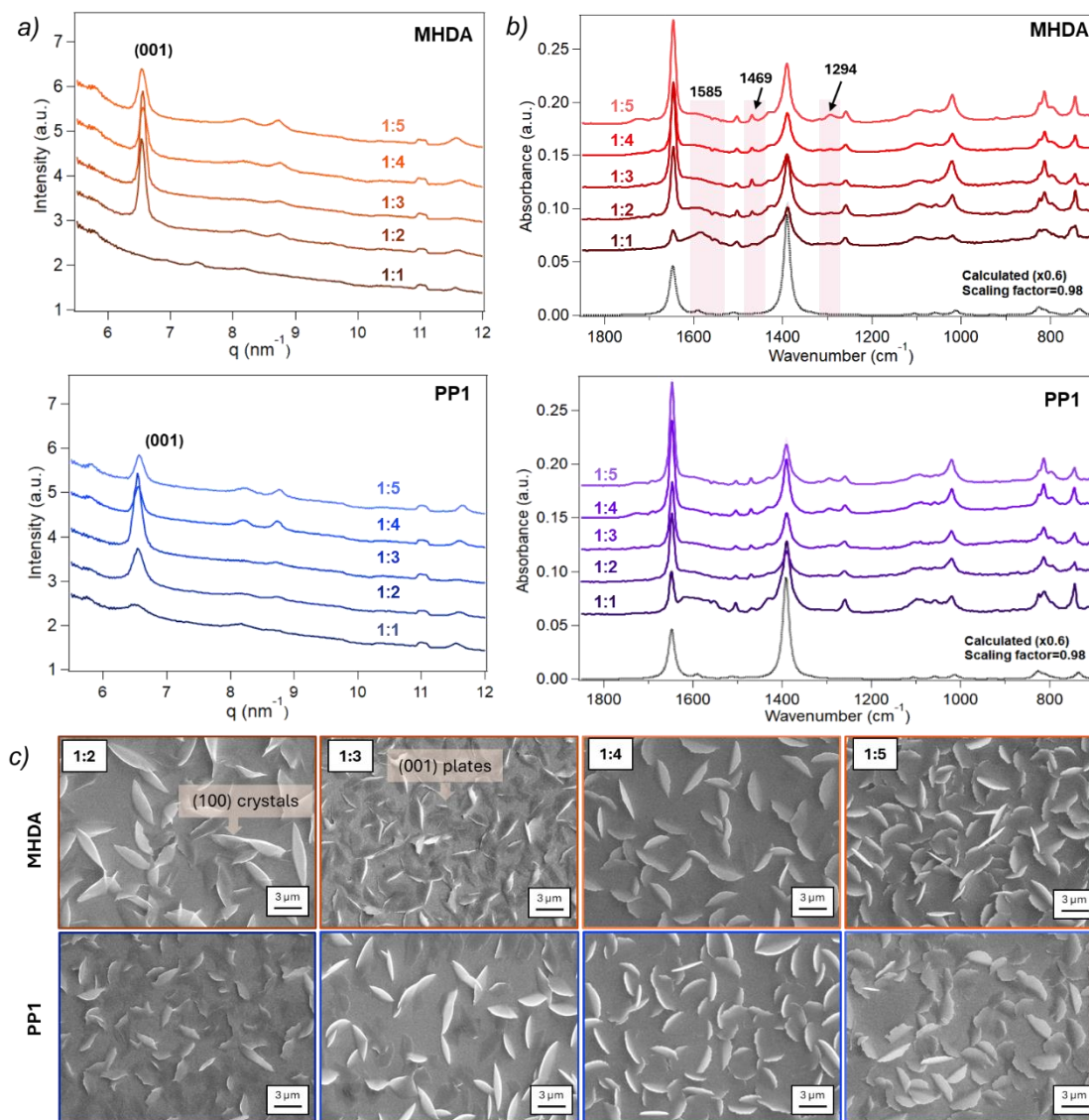


Figure 2. Characterization of Zn_2BDC_2DABCO thin films after 60 cycles grown on MHDA and PP1 functionalized substrates as a function of molar ratio (BDC:DABCO = 1:2/1:3/1:4/1:5) a) Radially integrated GIWAXS patterns; b) IR-spectra, calculated spectra is obtained from model structure V-exp.; c) SEM images of MOF films deposited on MHDA (top) and PP1 (bottom), at different BDC:DABCO ratio.

SEM imaging provides complementary insight into thin-film morphology (Figure 2 c), revealing that highly oriented films (BDC:DABCO ratios of 1:2 and 1:3) are composed of densely packed, plate-like crystallites aligned parallel to the substrate, in agreement with the dominant (001) out-of-plane orientation observed in GIWAXS. In contrast, films with higher isotropic contributions (BDC:DABCO ratios of 1:4 and 1:5) exhibit similarly shaped crystallites of comparable thickness but with a broad distribution of tilt angles relative to the substrate, giving rise to additional (100) crystallographic domains. This partial (100) alignment is also detectable in the GIWAXS patterns as almost negligible out-of-plane reflections (Figure S12 b). Such mixed-orientational growth behaviour has been reported previously in the $\text{Cu}_2(\text{F}_4\text{BDC})_2(\text{DABCO})$,^[37] where plate-like (001)-oriented structures were achieved by adjusting the synthesis temperature. The growth mechanism proposed by the authors involves twinning phenomena within the paddle-wheel nodes.^[37] According to this mechanism, in our case, structural defects arising from insufficient DABCO coordination at the ratio of BDC : DABCO = 1 : 2, allow some Zn_2 paddle-wheel units in the upper layers to rotate around the σ -bonds of the BDC linker. These rotated units act as nucleation sites, introducing distortions into crystals initially growing along the (001) direction. This results in the observed twinning in the films obtained herein, and is also consistent with previous observations in isostructural MOFs such as $\text{Cu}_2(\text{BDC})_2(\text{DABCO})$.^[54] Notably, at the molar ratio of BDC:DABCO = 1 : 3 this behavior is almost suppressed, considering that > 70% of the crystals align along the (001) reflection (*vide infra*, section 3.3).

Conversely, excessive DABCO competes with Zn^{2+} binding sites, suppressing formation of the Zn–BDC 2D sheets and promoting isotropic crystal orientations (Figure 2 c), which is in agreement with the observations for BDC:DABCO ratios of 1:4 and 1:5 (Figure 2 a). These results underscore the importance of careful stoichiometric optimization to achieve well-oriented MOF films with high structural alignment.

Upon increasing the number of deposition cycles to 120, a weak peak emerges at $q = 5.8 \text{ nm}^{-1}$, indicating the formation of (100)-oriented domains (Figure 3 a). In contrast, films deposited with 60 cycles show no additional peaks in the GIWAXS pattern. This behavior occurs irrespective of the linker molar ratio, as all samples with 120 cycles exhibit a broader distribution of crystallographic orientations (*vide infra*, Figure 6), likely resulting from cumulative layer-by-layer effects, including crystal twinning and excess DABCO (Figure 3 c). Here, early-stage (001)-oriented crystals serve as seeding nodes for the subsequent growth of tilted and (100)-oriented crystallites, as clearly shown in the cross-sectional SEM images (Figure S13).

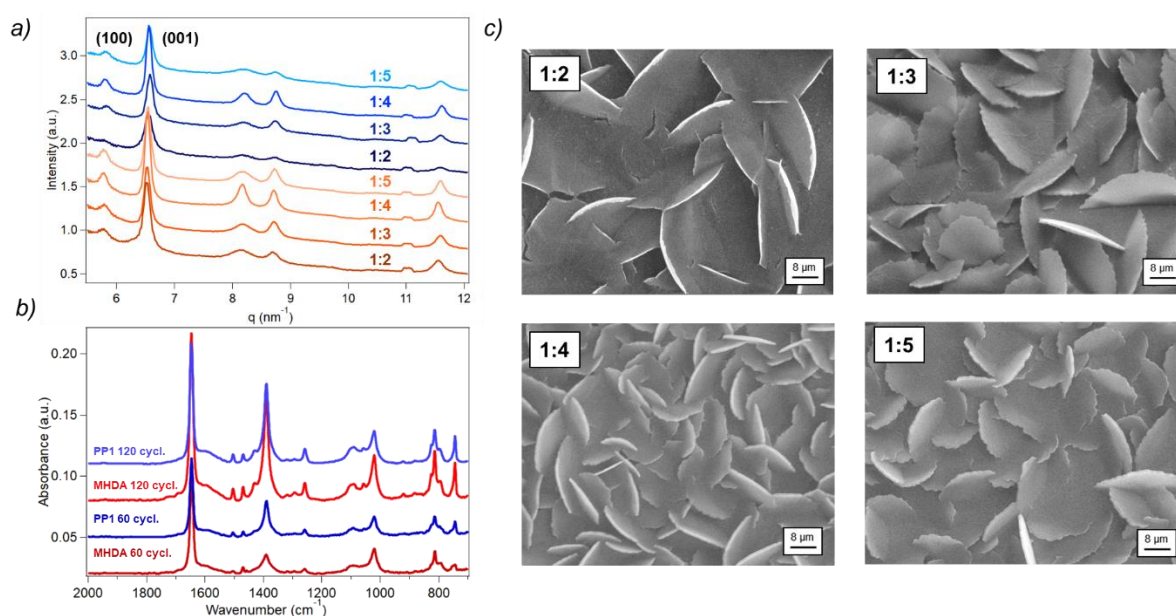


Figure 3. Characterization of $\text{Zn}_2\text{BDC}_2\text{DABCO}$ thin films after 120 cycles. a) Radially integrated GIWAXS patterns on MHDA (yellow) and PP1 (blue) functionalized substrates; b) IR-spectra of the BDC : DABCO = 1:3 ratio; c) SEM images of the films with different molar ratios.

Cross-sectional SEM images prepared by FIB-SEM (Figure S13 a,b) further reveal that both (001)- and (100)-oriented crystallites have similar thicknesses ($\sim 64 \text{ nm}$) and grow directly on top of the SAM layer. EDS and SEM analyses confirm that the regions between the crystallites

exhibit low metal content (Figure S13 b), indicating that MOF crystallite growth occurs through isolated islands, indicating a Volmer–Weber growth mechanism.^[13,54,55] These structural observations are complemented by analyzing the surface composition by ToF-SIMS, which provides detailed insight into the elemental and molecular composition of the films. Three-dimensional reconstructions show NH^- , C_6H_5^- , Au_3^- , and S^- signals, corresponding to nitrogen-containing moieties, aromatic fragments, gold from the substrate, and sulfur-containing species, respectively (**Figure 4 b,c**). Gas cluster ion beam (GCIB) sputter depth profiling of films with BDC:DABCO ratios of 1:3 and 1:5 revealed similar overall chemical composition and elemental distribution, with the exception of increased NH^- content in the 1:5 sample (Figure 4 a), reflecting the excess DABCO as identified in IR spectra (Figure 2 b). Sulphur species are predominantly enriched at the Au/MOF interface, consistent with the presence of the SAM, while Zn-related signals co-localize with C_6H_5^- fragments, confirming uniform incorporation of Zn within the aromatic MOF backbone.

Measuring a crater using 3D profilometry allowed the determination of the overall thickness of representative films with 1:3 and 1:5 ligand ratios, yielding 130 ± 15 nm (**Figure S14**). This total thickness includes ~ 50 nm of gold, ~ 10 nm of SAM, and ~ 70 nm of MOF, closely matching the crystal width observed by SEM.

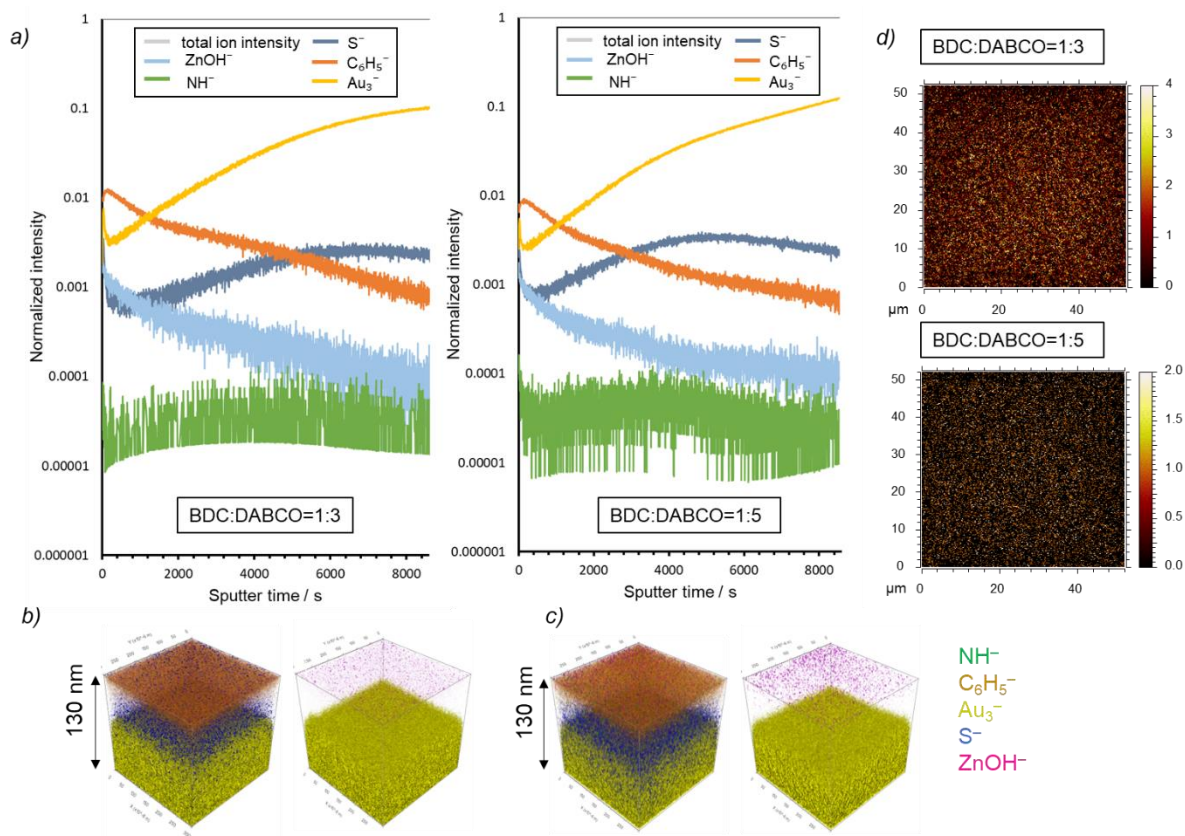


Figure 4. a) GCIB depth profiles showing the depth distribution of NH⁻, C₆H₅⁻, Au₃⁻, S⁻, and ZnOH⁻ signals displayed in the (b) and (c) three-dimensional ToF-SIMS reconstructions. (d) Two-dimensional ToF-SIMS images showing the distribution of the ZnOH⁻ signal on the MOF film surface (topmost position).

To further investigate whether the observed twinning could be either suppressed or enhanced, the metal-to-ligand ratio was systematically varied in films grown over 60 deposition cycles on MHDA self-assembled monolayer (**Figure 5**). Increasing the metal concentration with an equimolar ratio of BDC:DABCO=1:1 did not result in successful film growth, as expected considering the previous discussion of insufficient linker stoichiometry. Using the "optimal" ligand ratio of 1:3, decreasing the zinc acetate concentration to 0.05 mM produced well-oriented (001) samples, however, with poor film coverage, particularly at the sample edges. This limited coverage arises from insufficient material to coat the full substrate, as confirmed by SEM and GIR spectromicroscopy (Figure 5 b,c). In contrast, increasing the metal concentration to 0.2

mM yielded well-oriented (001) and uniform thin films. Further increasing the metal content beyond 0.3 mM led to a loss of preferential orientation, as clearly evidenced in the GIWAXS patterns (Figure 5 a).

These results demonstrate that the orientation of films fabricated via LbL-LPE spin-coating is primarily governed by synthetic conditions and can be achieved within short times under ambient conditions. To further demonstrate the robustness of the method and ensure reproducibility, the fraction of oriented crystallites was determined in the following section.

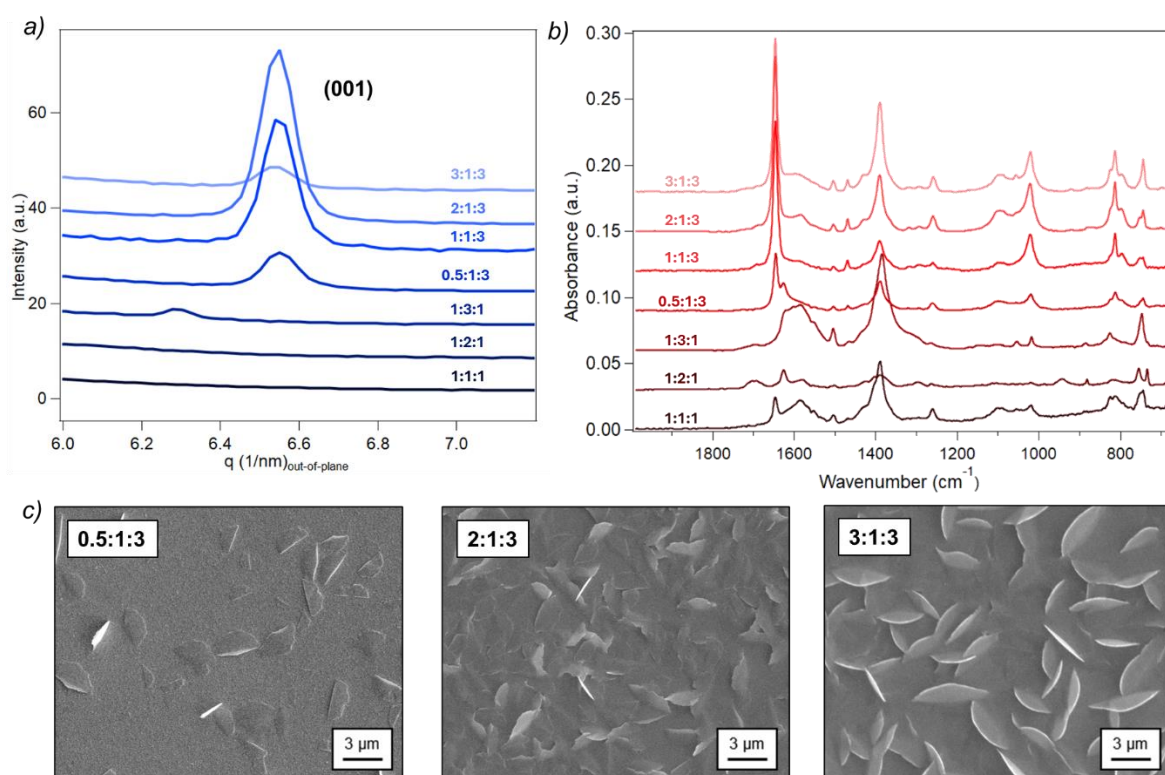


Figure 5. (a) GIWAXS, out-of-plane cut to compare (001) reflection, (b) IR, and (c) SEM data of the samples prepared by the variation of the Zn-BDC-DABCO molar ratios.

3.3. Quantitative analysis of film quality and reproducibility evaluation

To quantitatively assess the lattice alignment of Zn₂BDC₂DABCO thin films analyzed herein, the degree of orientation (DO) and Hermans orientation parameter (HOP) were evaluated from GIWAXS data. A detailed step-by-step description of the procedure is provided in the Supplementary Information, Chapter 9.^[56,57] While both parameters assess orientation in MOF

films, they reflect slightly different aspects. DO quantifies the fraction of crystallites that are oriented, with higher values indicating more homogeneous, well-aligned films, whereas lower values point to increased misalignment or heterogeneity. HOP complements this by providing an intensity-weighted measure of how sharply the crystallites are aligned over the azimuthal angle, enabling direct comparison of alignment quality between samples (**Figure S15**). Its values range from 1 (perfect alignment along the reference direction) to 0 (random orientation) and -0.5 (perfect alignment perpendicular to the reference direction). Both orientation parameters provide a clear measure of how the MOF lattice aligns with respect to the substrate and, because GIWAXS probes a relatively large area, they also reflect the overall homogeneity of the films. When combined with peak-width analysis (full width at half maximum, FWHM), it provides complementary information on film quality and allows evaluation of reproducibility across multiple samples. Only by including these parameters can a detailed interpretation of crystallite alignment be obtained, capturing both the overall film texture at the macroscale and the arrangement and shape of individual crystallites at the nanoscale. In contrast to one-dimensional out-of-plane GIWAXS scans or SEM micrographs, this quantification approach distinguishes oriented from isotropically distributed crystallite contributions. While MHDA- and PP1-functionalized films appear similarly in orientation and morphology from these simpler analyses, evaluation of DO and HOP reveals subtle but important structural differences. The mean value of DO for both MHDA- and PP1-functionalized samples, along with their standard deviations across replicate samples, are presented in **Table 1** and **Figure 6 a, b**. For films with a BDC:DABCO ratio of 1:3 on MHDA, excellent orientation is achieved with $DO=85\pm 10\%$ and HOP values of 0.9–1.0 (Figure S16). The narrow FWHM further indicates that the majority of crystallites are aligned parallel to the substrate surface. Lower ratios (1:2) result in a reduced mean value of DO ($65\pm 20\%$) and HOP = 0.75, accompanied by a large standard deviation, reflecting less homogeneous orientation. Higher ratios (1:4 and 1:5) show only a slight decrease in mean value of DO ($80\pm 5\%$) and HOP~0.8, but the substantially

increased FWHM indicates a broader distribution of orientations and reduced sharpness of out-of-plane alignment. PP1-functionalized films prepared with BDC:DABCO=1:3 exhibit a lower orientation along with a broad distribution indicative of reduced reproducibility ($DO = 60 \pm 20\%$, $HOP = 0.95$) compared to MHDA-functionalized films. Increasing the number of deposition cycles to 120 for MHDA films leaves the mean DO largely unchanged, but the FWHM increases, indicating that while the majority of crystallites remain preferentially aligned out-of-plane, an increased fraction becomes tilted as evidenced by SEM results (*vide supra*, Figure 3), leading to a broader azimuthal intensity distribution in GIWAXS. For PP1 functionalized samples, increasing the number of deposition cycles to 120 leads to a significant increase in FWHM (Figure 6 b) and a decrease in HOP (Figure S16 b).

Based on the correlative analysis of GIWAXS and IR results, as well as SEM observations, three representative alignment regimes for LbL-LPE fabricated Zn_2BDC_2DABCO films were identified and are schematically depicted in Figure 6d. For equimolar ligand ratios or BDC-rich conditions, crystal growth is minimal, and the MOF film remains largely amorphous. Gradually increasing the DABCO concentration up to 0.3 mM produces uniform films dominated by (001)-oriented crystallites. Further increases in DABCO concentrations up to 0.5 mM result in mixed crystal orientations due to twinning of the paddle-wheel units, leading to tilted and (100)-oriented crystallites. The reshaped 2D-GIWAXS patterns in Figure 6c illustrate the two extreme regimes. In the first case (Figure 6 c, *top*), a sharp (001) reflection indicates excellent orientation ($DO > 85\%$, $HP = 0.9-1$) with a narrow FWHM ($2 < 7^\circ$), showing that most crystallites align parallel to the substrate surface (central schematic, Figure 6d). This alignment is strongly observed for BDC:DABCO ratios of 1:3, partially for 1:2 and less for 1:4. In the second case (Figure 6 c, *bottom*), intensity spreads along the azimuthal angle χ , producing lower orientation ($DO < 85\%$, $HP = 0.8-0.9$) and significant broadening of the (001) reflection ($FWHM > 7^\circ$). This reflects partial misalignment as well as the presence of twinned crystallites with mixed (001)- and (100)-oriented domains (right schematic, Figure 6d), consistent with SEM

observations of tilted or standing crystallites. This was found for BDC:DABCO ratios of 1:4 and 1:5, as well as for films fabricated with 120 growth cycles, irrespective of the linker ratio. Considering these results, the BDC:DABCO ratio of 1:3 on an MHDA-functionalized surface with 60 synthesis cycles represents the optimal conditions for obtaining highly oriented films, evidencing that the herein developed LPE spin-coating protocol provides a suitable platform for the fabrication of robust and reproducible films. Moreover, comparing this data (DO=85±10%) with the degrees of orientation for the SHH-fabricated Zn₂BDC₂DABCO films seeded on Cu(BDC)₂ (45%)^[11] and seeded on Cu₂BDC₂DABCO (93%)^[26] underscores the effectiveness of the herein developed method, demonstrating that it enables high orientation without the need for complex templating or elaborate substrate preparation. The ability to achieve well-aligned films simply by adjusting the linker-to-linker and metal-to-linker ratios demonstrates that commercially available COOH-terminated thiols can be used directly for LbL-LPE growth, eliminating the need for pyridine-terminated SAMs, which require a lengthy synthesis and extensive purification (Supplementary information, chapter 1.3).^[36]

These results demonstrate that careful optimization of linker ratios, deposition cycles, SAM functionalization, spin-coating speed, solution volume, and deposition rate enables the reproducible fabrication of MOF thin films that combine high out-of-plane orientation, nanoscale crystallite alignment, and full macroscopic homogeneity. Together, these findings underscore the robustness, reproducibility, and scalability of the automated LbL-LPE spin-coating approach, establishing it as a reliable platform for the preparation of application-ready, highly ordered MOF thin films.

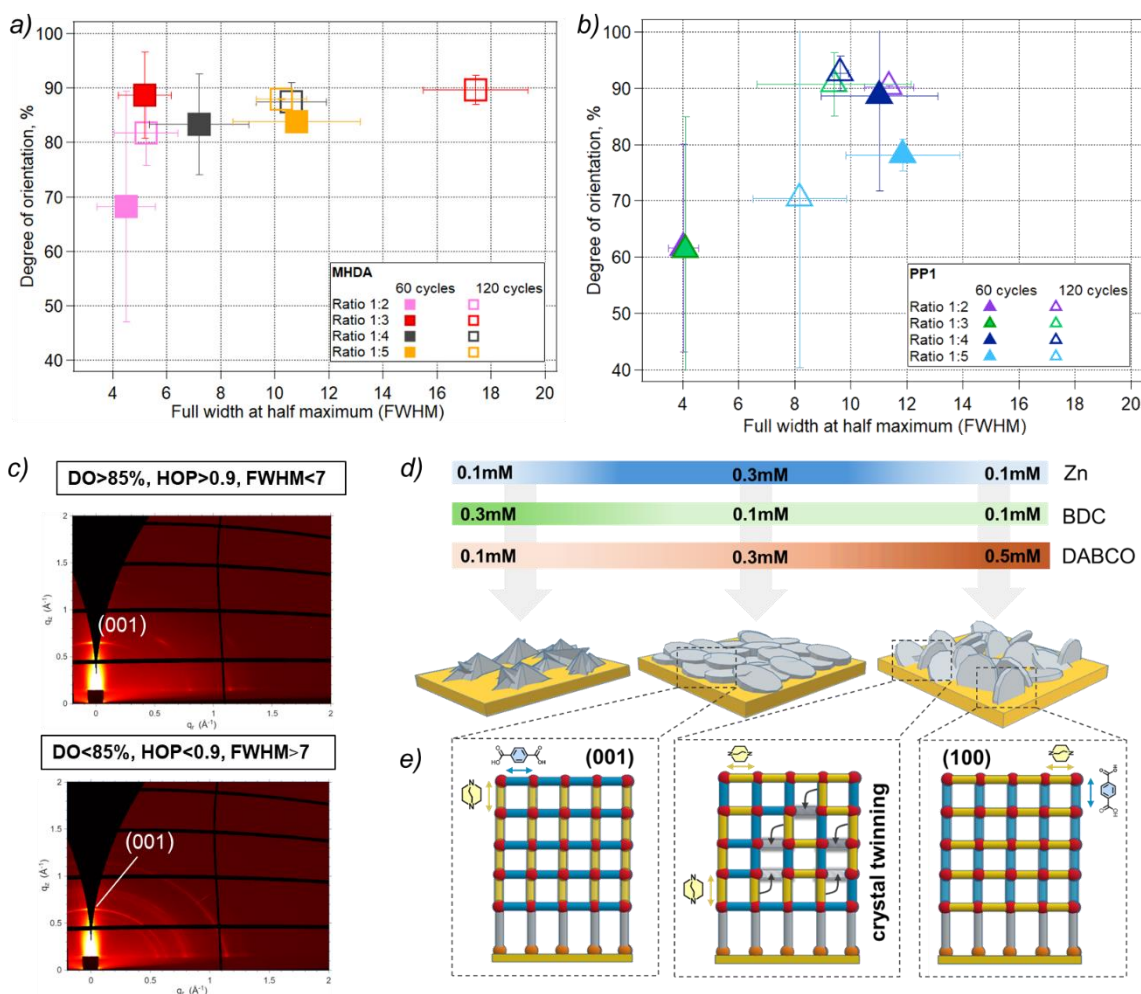


Figure 6. Degree of orientation versus peak width, where filled markers indicate 60 cycles and unfilled markers 120 cycles for (a) Mhda- and (b) PP1 functionalized samples. The degree of orientation and corresponding peak widths were averaged from triplicate samples (and from eight samples for the 1:3 ligand ratio at 60 cycles) under each synthetic condition. (c) Reshaped GIWAXS images showing highly oriented and isotropic scattering patterns. (d) Schematic representation of how changes in the molar ratio of reagents influence the crystalline orientation of LbL LPE-synthesized films. (e) Illustration of different crystalline orientations of MOF structures on a substrate.

4. Conclusion

This work reports the fully automated fabrication of mixed-linker, pillared-layered MOF thin films via LbL-LPE spin-coating under ambient, room-temperature conditions. Using the pillared-layered structure Zn_2BDC_2DABCO as a proof-of-concept, we demonstrate that exact

control over linker-to-linker and metal-to-linker ratios enables reproducible growth of chemically homogeneous, highly oriented films without the need for elevated temperatures or harmful solvents. An optimal Zn:BDC:DABCO ratio of 1:1:3 yields films with exceptional out-of-plane (001) lattice alignment ($DO > 85\%$), uniform coverage, and high crystallographic order. By carefully tuning linker and metal ratios, well-oriented MOF films can be achieved under the mild conditions inherently imposed by the spin-coating process, enabling enhanced environmental sustainability, efficient, and highly reproducible film formation with minimal reagent consumption.

Beyond achieving high crystallographic order, the automated LbL-LPE platform enables exact orientation control through regulation of critical process parameters, including SAM quality, reactant concentrations, deposition volume, and rotational speed. Quantitative analysis using GIWAXS, IR, and SEM confirms exceptional alignment along the surface normal, combined with homogeneous coverage across the substrate.

The present results demonstrate that this approach can be extended to more complex mixed-linker, pillared-layered systems with excellent film homogeneity and orientation control. The integration of full automation, room-temperature processing, low reagent consumption establishes LPE spin-coating as a robust and scalable platform for producing oriented MOF thin films that also addresses reproducibility challenges currently limiting reliable comparison and transferability of fabrication protocols across laboratories. The ability to obtain mixed-linker, pillared-layered MOFs with a high and quantifiable degree of orientation is particularly significant for orientation-dependent applications, where directional responses, thickness control, and reliable device integration are essential. More broadly, these findings provide a framework for extending automated LPE spin-coating to increasingly complex MOF architectures, opening new opportunities for their incorporation into functional materials and devices.

Acknowledgements

The authors acknowledge Ing. Andrea Radeticchio for technical support. The authors acknowledge the CERIC-ERIC consortium for access to the Austrian SAXS beamline in Elettra Synchrotron through proposals 20247158, 20247199, 20242148, 20242144, as well as the SISSI-Bio@Elettra for sharing their in-house beamtime and the financial support from the Slovenian Research Agency (P2-0118). The project is co-financed by the Republic of Slovenia, the Ministry of Education, Science and Sport, and the European Union under the European Regional Development Fund. Part of this work was supported by the Interreg Italy–Slovenia Programme (2021–2027, AllMICRO project). The authors would like to thank Gregor Kapun of the Nanocenter in Ljubljana for his valuable support with the cross-sectional analyses.

Data Availability Statement

((include as appropriate, including link to repository))

Received: ((will be filled in by the editorial staff))

Revised: ((will be filled in by the editorial staff))

Published online: ((will be filled in by the editorial staff))

References

- (1) Khalil, I. E.; Fonseca, J.; Reithofer, M. R.; Eder, T.; Chin, J. M. Tackling Orientation of Metal-Organic Frameworks (MOFs): The Quest to Enhance MOF Performance. *Coordination Chemistry Reviews* **2023**, *481*, 215043. <https://doi.org/10.1016/j.ccr.2023.215043>.
- (2) Gilroy, K. D.; Ruditskiy, A.; Peng, H.-C.; Qin, D.; Xia, Y. Bimetallic Nanocrystals: Syntheses, Properties, and Applications. *Chem. Rev.* **2016**, *116* (18), 10414–10472. <https://doi.org/10.1021/acs.chemrev.6b00211>.
- (3) Klokic, S.; Marmiroli, B.; Birarda, G.; Lackner, F.; Holzer, P.; Sartori, B.; Abbasgholiana, B.; Dal Zilio, S.; Kargl, R.; Stana Kleinschek, K.; Stani, C.; Vaccari, L.; Amenitsch, H. Flexible Metal-Organic Framework Films for Reversible Low-Pressure Carbon Capture and Release. *Nat Commun* **2025**, *16* (1), 7135. <https://doi.org/10.1038/s41467-025-60027-6>.
- (4) ZareKarizi, F.; Joharian, M.; Morsali, A. Pillar-Layered MOFs: Functionality, Interpenetration, Flexibility and Applications. *J. Mater. Chem. A* **2018**, *6* (40), 19288–19329. <https://doi.org/10.1039/C8TA03306D>.

- (5) Wannapaiboon, S.; Schneemann, A.; Hante, I.; Tu, M.; Epp, K.; Semrau, A. L.; Sternemann, C.; Paulus, M.; Baxter, S. J.; Kieslich, G.; Fischer, R. A. Control of Structural Flexibility of Layered-Pillared Metal–Organic Frameworks Anchored at Surfaces. *Nat Commun* **2019**, *10* (1), 346. <https://doi.org/10.1038/s41467-018-08285-5>.
- (6) Zhang, J.-P.; Zhou, H.-L.; Zhou, D.-D.; Liao, P.-Q.; Chen, X.-M. Controlling Flexibility of Metal–Organic Frameworks. *National Science Review* **2018**, *5* (6), 907–919. <https://doi.org/10.1093/nsr/nwx127>.
- (7) Senkovska, I.; Bon, V.; Abylgazina, L.; Mendt, M.; Berger, J.; Kieslich, G.; Petkov, P.; Luiz Fiorio, J.; Joswig, J.; Heine, T.; Schaper, L.; Bachetzky, C.; Schmid, R.; Fischer, R. A.; Pöpl, A.; Brunner, E.; Kaskel, S. Understanding MOF Flexibility: An Analysis Focused on Pillared Layer MOFs as a Model System. *Angew Chem Int Ed* **2023**, *62* (33), e202218076. <https://doi.org/10.1002/anie.202218076>.
- (8) Jin, E.; Bon, V.; Das, S.; Wonanke, A. D. D.; Etter, M.; Karlsen, M. A.; De, A.; Bönisch, N.; Heine, T.; Kaskel, S. Engineering Photoswitching Dynamics in 3D Photochromic Metal–Organic Frameworks through a Metal–Organic Polyhedron Design. *J. Am. Chem. Soc.* **2025**, *147* (10), 8568–8577. <https://doi.org/10.1021/jacs.4c17203>.
- (9) Falcaro, P.; Okada, K.; Hara, T.; Ikigaki, K.; Tokudome, Y.; Thornton, A. W.; Hill, A. J.; Williams, T.; Doonan, C.; Takahashi, M. Centimetre-Scale Micropore Alignment in Oriented Polycrystalline Metal–Organic Framework Films via Heteroepitaxial Growth. *Nature Mater* **2017**, *16* (3), 342–348. <https://doi.org/10.1038/nmat4815>.
- (10) Vinogradov, A. V.; Milichko, V. A.; Zaake-Hertling, H.; Aleksovska, A.; Gruschinski, S.; Schmorl, S.; Kersting, B.; Zolnhofer, E. M.; Sutter, J.; Meyer, K.; Lönnecke, P.; Hey-Hawkins, E. Unique Anisotropic Optical Properties of a Highly Stable Metal–Organic Framework Based on Trinuclear Iron(III) Secondary Building Units Linked by Tetracarboxylic Linkers with an Anthracene Core. *Dalton Trans.* **2016**, *45* (17), 7244–7249. <https://doi.org/10.1039/C6DT00390G>.
- (11) Klokic, S.; Naumenko, D.; Marmiroli, B.; Carraro, F.; Linares-Moreau, M.; Zilio, S. D.; Birarda, G.; Kargl, R.; Falcaro, P.; Amenitsch, H. Unraveling the Timescale of the Structural Photo-Response within Oriented Metal–Organic Framework Films. *Chem. Sci.* **2022**, *13* (40), 11869–11877. <https://doi.org/10.1039/D2SC02405E>.
- (12) Klokic, S.; Marmiroli, B.; Naumenko, D.; Birarda, G.; Dal Zilio, S.; Velásquez-Hernández, M. D. J.; Falcaro, P.; Vaccari, L.; Amenitsch, H. Orthogonal Stimulation of Structural Transformations in Photo-Responsive MOF Films through Linker Functionalization. *CrystEngComm* **2024**, *26* (17), 2228–2232. <https://doi.org/10.1039/D4CE00221K>.
- (13) Ehrling, S.; Miura, H.; Senkovska, I.; Kaskel, S. From Macro- to Nanoscale: Finite Size Effects on Metal–Organic Framework Switchability. *Trends in Chemistry* **2021**, *3* (4), 291–304. <https://doi.org/10.1016/j.trechm.2020.12.012>.
- (14) Zhai, M.; Moghadam, F.; Gosiamemang, T.; Heng, J. Y. Y.; Li, K. Facile Orientation Control of MOF-303 Hollow Fiber Membranes by a Dual-Source Seeding Method. *Nat Commun* **2024**, *15* (1), 10264. <https://doi.org/10.1038/s41467-024-54730-z>.
- (15) Talin, A. A.; Centrone, A.; Ford, A. C.; Foster, M. E.; Stavila, V.; Haney, P.; Kinney, R. A.; Szalai, V.; El Gabaly, F.; Yoon, H. P.; Léonard, F.; Allendorf, M. D. Tunable Electrical Conductivity in Metal–Organic Framework Thin-Film Devices. *Science* **2014**, *343* (6166), 66–69. <https://doi.org/10.1126/science.1246738>.

- (16) Okada, K.; Mori, K.; Fukatsu, A.; Takahashi, M. Oriented Growth of Semiconducting TCNQ@Cu₃ (BTC)₂ MOF on Cu(OH)₂: Crystallographic Orientation and Pattern Formation toward Semiconducting Thin-Film Devices. *J. Mater. Chem. A* **2021**, *9* (35), 19613–19618. <https://doi.org/10.1039/D1TA02968A>.
- (17) Xu, T.; Liu, Z.; Li, X.; Xu, T. The Evolution of Metal–Organic Framework Membranes: From Laboratory Innovation to Industrial Implementations. *Ind. Eng. Chem. Res.* **2025**, *64* (20), 9847–9866. <https://doi.org/10.1021/acs.iecr.5c00781>.
- (18) Shrivastav, V.; Mansi; Gupta, B.; Dubey, P.; Deep, A.; Nogala, W.; Shrivastav, V.; Sundriyal, S. Recent Advances on Surface Mounted Metal–Organic Frameworks for Energy Storage and Conversion Applications: Trends, Challenges, and Opportunities. *Advances in Colloid and Interface Science* **2023**, *318*, 102967. <https://doi.org/10.1016/j.cis.2023.102967>.
- (19) Halder, R.; Heinke, L.; Wöll, C. Advanced Photoresponsive Materials Using the Metal–Organic Framework Approach. *Advanced Materials* **2020**, *32* (20), 1905227. <https://doi.org/10.1002/adma.201905227>.
- (20) Kolodzeiski, E.; Amirjalayer, S. Dynamic Network of Intermolecular Interactions in Metal–Organic Frameworks Functionalized by Molecular Machines. *Science Advances* **2022**, *8* (26), eabn4426. <https://doi.org/10.1126/sciadv.abn4426>.
- (21) Xiao, Y.-H.; Tian, Y.-B.; Gu, Z.-G.; Zhang, J. Surface-Coordinated Metal–Organic Framework Thin Films (SURMOFs): From Fabrication to Energy Applications. *EnergyChem* **2021**, *3* (6), 100065. <https://doi.org/10.1016/j.enchem.2021.100065>.
- (22) Shekhah, O.; Wang, H.; Kowarik, S.; Schreiber, F.; Paulus, M.; Tolan, M.; Sternemann, C.; Evers, F.; Zacher, D.; Fischer, R. A.; Wöll, C. Step-by-Step Route for the Synthesis of Metal–Organic Frameworks. *J. Am. Chem. Soc.* **2007**, *129* (49), 15118–15119. <https://doi.org/10.1021/ja076210u>.
- (23) Zhuang, J.-L.; Terfort, A.; Wöll, C. Formation of Oriented and Patterned Films of Metal–Organic Frameworks by Liquid Phase Epitaxy: A Review. *Coordination Chemistry Reviews* **2016**, *307*, 391–424. <https://doi.org/10.1016/j.ccr.2015.09.013>.
- (24) Makiura, R.; Motoyama, S.; Umemura, Y.; Yamanaka, H.; Sakata, O.; Kitagawa, H. Surface Nano-Architecture of a Metal–Organic Framework. *Nature Mater* **2010**, *9* (7), 565–571. <https://doi.org/10.1038/nmat2769>.
- (25) Linares-Moreau, M.; Brandner, L. A.; Kamencek, T.; Klokic, S.; Carraro, F.; Okada, K.; Takahashi, M.; Zojer, E.; Doonan, C. J.; Falcaro, P. Semi-Automatic Deposition of Oriented Cu(OH)₂ Nanobelts for the Heteroepitaxial Growth of Metal–Organic Framework Films. *Adv Materials Inter* **2021**, *8* (21), 2101039. <https://doi.org/10.1002/admi.202101039>.
- (26) Zhao, T.; Taghizade, N.; Fischer, J. C.; Richards, B. S.; Howard, I. A. [001]-Oriented Heteroepitaxy for Fabricating Emissive Surface Mounted Metal–Organic Frameworks. *J. Mater. Chem. C* **2024**, *12* (15), 5496–5505. <https://doi.org/10.1039/D4TC00018H>.
- (27) Romero-Ángel, M.; Rubio-Giménez, V.; Gómez-Oliveira, E. P.; Verstreken, M. F. K.; Smets, J.; Gándara-Loe, J.; M Padial, N.; Ameloot, R.; Tatay, S.; Martí-Gastaldo, C. Vapor-Assisted Conversion of Heterobimetallic Titanium–Organic Framework Thin Films. *Chem. Mater.* **2023**, *35* (24), 10394–10402. <https://doi.org/10.1021/acs.chemmater.3c01389>.
- (28) Bétard, A.; Fischer, R. A. Metal–Organic Framework Thin Films: From Fundamentals to Applications. *Chem. Rev.* **2012**, *112* (2), 1055–1083. <https://doi.org/10.1021/cr200167v>.

- (29) Sabzehmeidani, M. M.; Gafari, S.; Jamali, S.; Kazemzad, M. Concepts, Fabrication and Applications of MOF Thin Films in Optoelectronics: A Review. *Applied Materials Today* **2024**, *38*, 102153. <https://doi.org/10.1016/j.apmt.2024.102153>.
- (30) Shi, X.; Shan, Y.; Du, M.; Pang, H. Synthesis and Application of Metal-Organic Framework Films. *Coordination Chemistry Reviews* **2021**, *444*, 214060. <https://doi.org/10.1016/j.ccr.2021.214060>.
- (31) Chernikova, V.; Shekhah, O.; Eddaoudi, M. Advanced Fabrication Method for the Preparation of MOF Thin Films: Liquid-Phase Epitaxy Approach Meets Spin Coating Method. *ACS Appl. Mater. Interfaces* **2016**, *8* (31), 20459–20464. <https://doi.org/10.1021/acsami.6b04701>.
- (32) Jiang, H.; Staeglich, B.; Knoch, J.; Kumar, S.; Dilbaghi, N.; Deep, A.; Ingebrandt, S.; Pachauri, V. Programming Layer-by-Layer Liquid Phase Epitaxy in Microfluidics for Realizing Two-Dimensional Metal–Organic Framework Sensor Arrays. *Environ. Sci.: Nano* **2025**, *12* (3), 1849–1857. <https://doi.org/10.1039/D4EN00764F>.
- (33) Fischer, J. C.; Steentjes, R.; Chen, D.-H.; Richards, B. S.; Zojer, E.; Wöll, C.; Howard, I. A. Determining Structures of Layer-by-Layer Spin-Coated Zinc Dicarboxylate-Based Metal-Organic Thin Films. *Chemistry – A European Journal* **2024**, *30* (37), e202400565. <https://doi.org/10.1002/chem.202400565>.
- (34) Prue, A. A.; Chalmers, A. T.; Anderson, H. C.; Ralph, A. D.; Smith, S. J.; Stowers, K. J. Flexible and Rapid Synthesis of Bimetallic Metal–Organic Framework Thin Films. *Crystal Growth & Design* **2025**, *25* (9), 2849–2856. <https://doi.org/10.1021/acs.cgd.4c01461>.
- (35) Kitagawa, S.; Kitaura, R.; Noro, S. Functional Porous Coordination Polymers. *Angewandte Chemie International Edition* **2004**, *43* (18), 2334–2375. <https://doi.org/10.1002/anie.200300610>.
- (36) Shekhah, O. Layer-by-Layer Method for the Synthesis and Growth of Surface Mounted Metal-Organic Frameworks (SURMOFs). *Materials* **2010**, *3* (2), 1302–1315. <https://doi.org/10.3390/ma3021302>.
- (37) Zhuang, J.-L.; Kind, M.; Grytz, C. M.; Farr, F.; Diefenbach, M.; Tussupbayev, S.; Holthausen, M. C.; Terfort, A. Insight into the Oriented Growth of Surface-Attached Metal–Organic Frameworks: Surface Functionality, Deposition Temperature, and First Layer Order. *J. Am. Chem. Soc.* **2015**, *137* (25), 8237–8243. <https://doi.org/10.1021/jacs.5b03948>.
- (38) Liu, J.; Wöll, C. Surface-Supported Metal–Organic Framework Thin Films: Fabrication Methods, Applications, and Challenges. *Chem. Soc. Rev.* **2017**, *46* (19), 5730–5770. <https://doi.org/10.1039/C7CS00315C>.
- (39) Srisombat, L.; Jamison, A. C.; Lee, T. R. Stability: A Key Issue for Self-Assembled Monolayers on Gold as Thin-Film Coatings and Nanoparticle Protectants. *Colloids and Surfaces A: Physicochemical and Engineering Aspects* **2011**, *390* (1–3), 1–19. <https://doi.org/10.1016/j.colsurfa.2011.09.020>.
- (40) Willey, T. M.; Vance, A. L.; Van Buuren, T.; Bostedt, C.; Terminello, L. J.; Fadley, C. S. Rapid Degradation of Alkanethiol-Based Self-Assembled Monolayers on Gold in Ambient Laboratory Conditions. *Surface Science* **2005**, *576* (1–3), 188–196. <https://doi.org/10.1016/j.susc.2004.12.022>.
- (41) Jones, J. A.; Qin, L. A.; Meyerson, H.; Kwon, I. K.; Matsuda, T.; Anderson, J. M. Instability of Self-assembled Monolayers as a Model Material System for Macrophage/FBGC

Cellular Behavior. *J Biomedical Materials Res* **2008**, *86A* (1), 261–268. <https://doi.org/10.1002/jbm.a.31660>.

(42) Brewer, N. J.; Janusz, S.; Critchley, K.; Evans, S. D.; Leggett, G. J. Photooxidation of Self-Assembled Monolayers by Exposure to Light of Wavelength 254 Nm: A Static SIMS Study. *J. Phys. Chem. B* **2005**, *109* (22), 11247–11256. <https://doi.org/10.1021/jp0443299>.

(43) Singh, M.; Kaur, N.; Comini, E. The Role of Self-Assembled Monolayers in Electronic Devices. *J. Mater. Chem. C* **2020**, *8* (12), 3938–3955. <https://doi.org/10.1039/D0TC00388C>.

(44) Yang, E.; Song, X.-C.; Zhu, J.-W. 1,4-Diazoniabicyclo[2.2.2]Octane Terephthalate. *Acta Crystallogr E Struct Rep Online* **2008**, *64* (9), o1764–o1764. <https://doi.org/10.1107/S1600536808025312>.

(45) Gattorno, G. R.; Oskam, G. Forced Hydrolysis vs Self-Hydrolysis of Zinc Acetate in Ethanol and Iso-Butanol. *ECS Trans.* **2006**, *3* (9), 23–28. <https://doi.org/10.1149/1.2357093>.

(46) Kirlikovali, K. O.; Hanna, S. L.; Son, F. A.; Farha, O. K. Back to the Basics: Developing Advanced Metal–Organic Frameworks Using Fundamental Chemistry Concepts. *ACS Nanosci. Au* **2023**, *3* (1), 37–45. <https://doi.org/10.1021/acsnanoscienceau.2c00046>.

(47) Qi, X.; Xie, Y.; Niu, J.; Zhao, J.; Li, Y.; Fang, W.; Zhang, J. Application of Hard and Soft Acid-base Theory to Construct Heterometallic Materials with Metal-oxo Clusters. *Angew Chem Int Ed* **2025**, *64* (1), e202417548. <https://doi.org/10.1002/anie.202417548>.

(48) Zheng, S.; Sun, Y.; Xue, H.; Braunstein, P.; Huang, W.; Pang, H. Dual-Ligand and Hard-Soft-Acid-Base Strategies to Optimize Metal–Organic Framework Nanocrystals for Stable Electrochemical Cycling Performance. *National Science Review* **2022**, *9* (7), nwab197. <https://doi.org/10.1093/nsr/nwab197>.

(49) Gao, Q.; Xie, Y.-B.; Li, J.-R.; Yuan, D.-Q.; Yakovenko, A. A.; Sun, J.-H.; Zhou, H.-C. Tuning the Formations of Metal–Organic Frameworks by Modification of Ratio of Reactant, Acidity of Reaction System, and Use of a Secondary Ligand. *Crystal Growth & Design* **2012**, *12* (1), 281–288. <https://doi.org/10.1021/cg201059d>.

(50) Tang, Y.; Dubbeldam, D.; Tanase, S. Water–Ethanol and Methanol–Ethanol Separations Using in Situ Confined Polymer Chains in a Metal–Organic Framework. *ACS Appl. Mater. Interfaces* **2019**, *11* (44), 41383–41393. <https://doi.org/10.1021/acsami.9b14367>.

(51) Lugier, O.; Pokharel, U.; Castellanos, S. Impact of Synthetic Conditions on the Morphology and Crystallinity of FDMOF-1(Cu) Thin Films. *Crystal Growth & Design* **2020**, *20* (8), 5302–5309. <https://doi.org/10.1021/acs.cgd.0c00529>.

(52) Kovalenko, V. I.; Akhmadiyarov, A. A.; Vandyukov, A. E.; Khamatgalimov, A. R. Experimental Vibrational Spectra and Computational Study of 1,4-Diazabicyclo[2.2.2]Octane. *Journal of Molecular Structure* **2012**, *1028*, 134–140. <https://doi.org/10.1016/j.molstruc.2012.06.045>.

(53) Dybtsev, D. N.; Chun, H.; Kim, K. Rigid and Flexible: A Highly Porous Metal–Organic Framework with Unusual Guest-Dependent Dynamic Behavior. *Angew Chem Int Ed* **2004**, *43* (38), 5033–5036. <https://doi.org/10.1002/anie.200460712>.

(54) McCarthy, B. D.; Liseev, T.; Beiler, A. M.; Materna, K. L.; Ott, S. Facile Orientational Control of M₂L₂P SURMOFs on ⟨100⟩ Silicon Substrates and Growth Mechanism Insights for Defective MOFs. *ACS Appl. Mater. Interfaces* **2019**, *11* (41), 38294–38302. <https://doi.org/10.1021/acsami.9b12407>.

(55) Brandner, L. A.; Linares-Moreau, M.; Zhou, G.; Amenitsch, H.; Dal Zilio, S.; Huang, Z.; Doonan, C.; Falcaro, P. Water Sensitivity of Heteroepitaxial Cu-MOF Films: Dissolution and Re-Crystallization of 3D-Oriented MOF Superstructures. *Chem. Sci.* **2023**, *14* (43), 12056–12067. <https://doi.org/10.1039/D3SC04135B>.

(56) Fischer, J. C.; Li, C.; Hamer, S.; Heinke, L.; Herges, R.; Richards, B. S.; Howard, I. A. GIWAXS Characterization of Metal–Organic Framework Thin Films and Heterostructures: Quantifying Structure and Orientation. *Adv Materials Inter* **2023**, *10* (11), 2202259. <https://doi.org/10.1002/admi.202202259>.

(57) Oesinghaus, L.; Schlipf, J.; Giesbrecht, N.; Song, L.; Hu, Y.; Bein, T.; Docampo, P.; Müller-Buschbaum, P. Toward Tailored Film Morphologies: The Origin of Crystal Orientation in Hybrid Perovskite Thin Films. *Adv Materials Inter* **2016**, *3* (19), 1600403. <https://doi.org/10.1002/admi.201600403>.

Automatic LbL-LPE Spin-Coating Strategy for the Fabrication of Highly Oriented Mixed-Linker MOF Thin Films for Orientation-Dependent Applications

SUPPLEMENTARY INFORMATION

Eleonora Afanasenko,¹ Benedetta Marmiroli,² Behnaz Abbasgholi-NA,³ Barbara Sartori², Giovanni Birarda,⁴ Chiaramaria Stani,⁴ Matjaž Finšgar,⁵ Peter E. Hartmann,⁶ Mark Bieber,⁷ Emma Walitsch,⁷ Rolf Breinbauer,⁷ Simone Dal Zilio,³ Sumea Klokic^{2*} and Heinz Amenitsch^{2*}

- 1 CERIC-ERIC, Trieste, Italy
- 2 Institute of Inorganic Chemistry, University of Technology, Graz, Austria
- 3 Istituto Officina dei Materiali - CNR-IOM, Trieste, Italy
- 4 Elettra Sincrotrone Trieste, Trieste, Italy
- 5 Faculty of chemistry and chemical engineering, University of Maribor, Slovenia
- 6 Institute of Physical and Theoretical Chemistry University of Graz, Austria
- 7 Institute of Organic Chemistry, University of Technology, Graz, Austria

Table of contents

1. Experiment	3
1.1. Materials and methods	3
1.2. Synthesis of the Zn ₂ BDC ₂ DABCO thin films.....	3
1.3. Synthesis of the 4-(4-pyridyl)phenyl)methanethiol (PP1).....	4
1.2. Characterization techniques	8
1.2.1. Grazing Incidence Small Angle X-Ray Scattering (GIWAXS) Experiments	8
1.2.2. IR spectromicroscopy.....	8
1.2.3. SEM and EDS measurements	8
1.2.4. ToF-SIMS measurements.....	8
2. LPE Spin-Coating Workflow	10
3. Assessment of film uniformity and fabrication reproducibility	12
4. GIWAXS Characterization of Zn ₂ (BDC) ₂ (DABCO) Films	25
5. DFT calculations.....	14
5.1. Computational Details.....	14
5.2. Detailed Information on the Computations.....	15
6. Calculated vs. experimental IR spectra and vibrational peaks assignment	23
7. Surface and cross-section morphology	25
8. Thin film thickness measurement with 3D profilometry	27
9. Degree of orientation and Hermans orientation parameter calculations.....	28
References.....	32

1. Experiment

1.1. Materials and methods

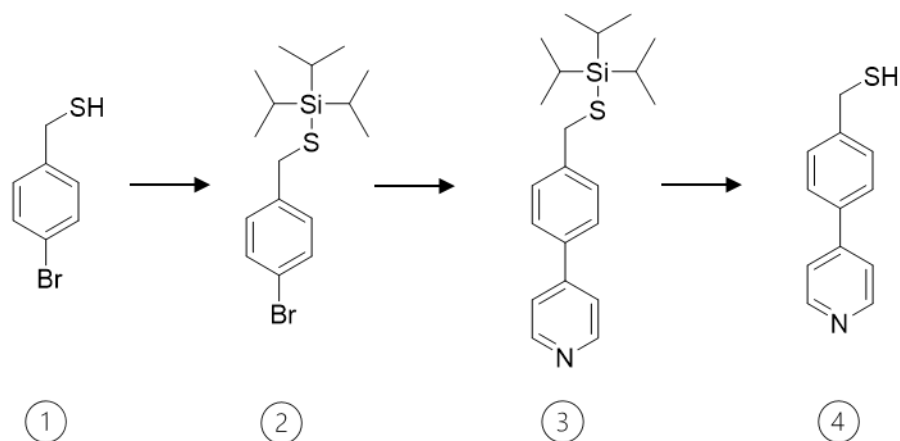
Reagents and solvents are available commercially and were used as received without any further purification. The linkers benzene-1,4-dicarboxylic acid (BDC), 1,4-Diazabicyclo[2.2.2]octane (DABCO) as well as the 16-Mercaptohexadecanoic acid for the SAM were purchased from TCI Chemicals, while zinc acetate dihydrate was obtained from TCI Chemicals, absolute ethanol (EtOH, 99.8%) was bought from VWR Chemicals. Gold-deposited substrates (polycrystalline gold with thickness on Si substrate precoated with titanium, roughness < 1nm) were purchased from Georg Albert PVD-Beschichtungen. The spin-coating step was performed using a Laurell spinner (Model WS-650MZ-23NPPB), Norm-Ject 20 mL plastic syringes with a standard diameter of 19.4 mm, and programmable syringe pumps (Harvard PHD 4400). Experiments were performed at ambient conditions.

1.2. Synthesis of the Zn_2BDC_2DABCO thin films

Self-assembled monolayers (SAMs) were formed on gold substrates by immersion in an ethanolic (absolute) 0.02 mM solution of 16-mercaptohexadecanoic acid (MHDA) containing 10 vol% acetic acid, or in a 0.02 mM solution of (4-(4-pyridyl)phenyl)methanethiol (PP1), for 24 hours. Prior to functionalization, the wafers were sonicated in absolute ethanol for 30 minutes to ensure thorough cleaning.

The linker working solution was prepared by dissolving 0.01 mmol of benzene-1,4-dicarboxylic acid (BDC) in 100 mL of ethanol and sonicating for 2 hours to ensure complete dissolution. After confirming the proper BDC concentration via UV-Vis spectroscopy, 0.03 mmol of 1,4-diazabicyclo[2.2.2]octane (DABCO) was added, and the solution was sonicated for an additional hour. The metal working solution was prepared by dissolving 0.01 mmol of $Zn(CH_3CO_2)_2 \cdot 2H_2O$ in 100 mL of ethanol, followed by 1 hour of sonication.

1.3. Synthesis of the 4-(4-pyridyl)phenyl)methanethiol (PP1)



1) (4-Bromophenyl)methanethiol

17.0 g 4-bromobenzylbromide (68.0 mmol, 1 equiv.) were dissolved in MeOH (150 mL). Afterwards, 8.55 g potassium thioacetate (74.8 mmol, 1.1 equiv.) were added and the resulting suspension was stirred at r.t. for 30 min in an argon-flushed three-necked round-bottom flask, equipped with a Teflon-coated magnetic stirring bar. After TLC and GC-MS indicated full conversion, 9.41 g K_2CO_3 (68.1 mmol, 1 equiv.) were added and the suspension was stirred for another 40 min at r.t. After complete consumption of the intermediate thioacetate (reaction monitoring via TLC and GC-MS), the reaction mixture was carefully acidified (pH = 6) with 1M aq. HCl and extracted with DCM (3 x 120 mL). The combined organic phases were dried over Na_2SO_4 , filtered and concentrated under reduced pressure. The crude product was used in the next step without further purification.

Yield: 13.8 g (quant.), orange oil, C_7H_7BrS [203.10 g/mol].

TLC: $R_f = 0.75$ (cyclohexane:EtOAc = 9:1; UV).

GC-MS: (EI, 70 eV; MT_50_S): $t_R = 5.22$ min; m/z (%): 204 (26), 169 (100), 121 (6), 90 (30), 63 (12).

1H NMR (300 MHz, $CDCl_3$): δ 7.44 (d, $J = 8.3$ Hz, 2H), 7.20 (d, $J = 8.3$ Hz, 2H), 3.69 (d, $J = 7.6$ Hz, 2H), 1.76 (t, $J = 7.6$ Hz, 1H; -SH) ppm.

^{13}C NMR (76 MHz, $CDCl_3$): δ 140.2, 131.9, 129.9, 121.0, 28.5 ppm.

2) ((4-Bromobenzyl)thio)triisopropylsilane

An argon-flushed Schlenk flask, equipped with a Teflon-coated magnetic stirring bar, was charged with 11.6 g (4-bromophenyl)methanethiol (57.1 mmol, 1 equiv.) and dissolved in abs. THF (110 mL). The reaction mixture was cooled to 0 °C and 2.51 g NaH (62.8 mmol, 1.1 equiv.) were added in portions over 15 min. The Schlenk flask was equipped with a bubbler and the reaction mixture was stirred until the evolution of gas had ceased (50 min). Afterwards, 13 mL TIPSCI (62.8 mmol, 1.1 equiv.) were added dropwise over 15 min and the reaction mixture was stirred for 70 min at r.t. (reaction monitoring via GC-MS). Subsequently, the reaction was quenched by the addition of H₂O (110 mL). The phases were separated and the aqueous phase was back-extracted with EtOAc (3 x 110 mL). The combined organic phases were dried over Na₂SO₄, filtered and concentrated under reduced pressure. The crude product was first purified via vacuum distillation (10.0 x 2.0 cm Vigreux column, 0.041 mbar) and then via flash column chromatography (1 L SiO₂, 26.0 x 8.0 cm, cyclohexane to cyclohexane:EtOAc = 10:1 (v/v)).

Yield: 13.5 g (66%), colourless liquid, C₁₆H₂₇BrSSi [359.44 g/mol].

TLC: R_f = 0.39 (cyclohexane; UV).

b.p: 119-120 °C (0.041 mbar).

GC-MS: (EI, 70 eV; MT_50_S): t_R = 7.69 min; m/z (%): 360 (1), 315 (50), 273 (7), 169 (100), 90 (24).

¹H NMR (300 MHz, CDCl₃): δ 7.42 (d, J = 8.3 Hz, 2H), 7.22 (d, J = 8.3 Hz, 2H), 3.69 (s, 2H), 1.30 (hept, J = 7.1 Hz, 3H), 1.13 (d, J = 7.1 Hz, 18H) ppm.

¹³C NMR (76 MHz, CDCl₃): δ 140.0, 131.7, 130.3, 120.7, 29.7, 18.71, 12.9 ppm.

3) 4-(4-(((Triisopropylsilyl)thio)methyl)phenyl)pyridine

An argon-flushed Schlenk flask, equipped with a Teflon-coated magnetic stirring bar, was charged with 1.67 g 4-pyridylboronic acid (90% purity, 12.2 mmol, 1.2 equiv.), 6.67 g CsCO₃ (20.5 mmol, 2 equiv.), 374 mg Pd(dppf)Cl₂ (0.512 mmol, 0.05 equiv.), 370 μL H₂O (20.5 mmol, 2 equiv.) and 3.66 g ((4-bromobenzyl)thio)triisopropylsilane (10.2 mmol, 1 equiv.) and dissolved in degassed 1,4-dioxane (30 mL). Then, the reaction mixture was stirred at 90 °C for 20 h. After complete consumption of the starting material (reaction monitoring via GC-MS), the reaction mixture was cooled to r.t.. The

mixture was taken up in H₂O (30 mL) and extracted with EtOAc (4 x 30 mL). The combined organic phases were dried over Na₂SO₄, filtered and concentrated under reduced pressure. The crude product was purified via flash column chromatography (500 mL SiO₂, 20.0 x 6.0 cm, cyclohexane:EtOAc = 4:1 (v/v) to cyclohexane:EtOAc = 1:1 (v/v)).

Yield: 2.99 g (83%), beige, waxy solid, C₂₁H₃₁NSSi [357.63 g/mol].

TLC: R_f = 0.45 (cyclohexane:EtOAc = 1:1; UV, KMnO₄).

GC-MS: (EI, 70 eV; MT_50_S): t_R = 9.80 min; m/z (%): 357 (10), 314 (49), 168 (100), 139 (3), 115 (5).

¹H NMR (300 MHz, CD₂Cl₂): δ 8.68 – 8.57 (m, 2H), 7.62 (d, *J* = 8.1 Hz, 2H), 7.55 – 7.43 (m, 4H), 3.81 (s, 2H), 1.40 – 1.25 (m, 3H), 1.16 (d, *J* = 7.2 Hz, 18H) ppm.

¹³C NMR (76 MHz, CD₂Cl₂): δ 150.8, 148.3, 142.8, 137.2, 129.8, 127.6, 121.9, 30.3, 18.9, 13.3 ppm.

4) (4-(Pyridin-4-yl)phenyl)methanethiol

Two batches have been prepared consecutively as described in the following procedure:

In an argon-flushed 500 mL two-necked round-bottom flask, equipped with a Teflon-coated magnetic stirring bar, a mixture of MeOH (150 mL) and 6M aq. HCl (30 mL) were degassed by passing a stream of nitrogen through the solution for 1 h. Afterwards, 2.60 g 4-(4-(((triisopropylsilyl)thio)methyl)phenyl)pyridine (7.27 mmol, 1 equiv.) were added and the mixture was heated under reflux for 20 h. The reaction mixture was allowed to cool to r.t. and diluted with a mixture of MeOH and H₂O (150 mL; 1:1 (v/v)). The mixture was washed with *n*-pentane (1 x 50 mL, 2 x 100 mL) to remove apolar impurities before the MeOH was removed under reduced pressure. The resulting aqueous solution was again degassed by sonication and passing a stream of nitrogen through the solution for 15 min. Afterwards, the pH of the solution was adjusted to pH ~6 by the addition of solid trisodium citrate dihydrate. The slurry was immediately extracted with DCM (3 x 100 mL). The combined organic phases were dried over Na₂SO₄, filtered and concentrated under reduced pressure. The crude product was dissolved in boiling, degassed methyl cyclohexane (250 mL), filtered hot through a Schlenk frit and left for crystallization. The crystals were collected by filtration, washed

with *n*-pentane and dried *in vacuo*. Further purification was performed by evaporation and resublimation on a cooling finger (105 °C, 0.15 mbar).

Yield: 2.09 g (53% (2 batches)), colourless solid, C₁₂H₁₁NS [201.29 g/mol].

GC-MS: (EI, 70 eV; MT_50_S): t_R = 6.97 min; *m/z* (%): 201 (18), 168 (100), 139 (8), 63 (5).

m.p. = 62-64 °C.

¹H NMR (400 MHz, CDCl₃): δ 8.67 – 8.62 (m, 2H), 7.62 – 7.57 (m, 2H), 7.52 – 7.47 (m, 2H), 7.46 – 7.41 (m, 2H), 3.79 (d, *J* = 7.6 Hz, 2H), 1.81 (t, *J* = 7.6 Hz, 1H; -SH) ppm.

¹³C NMR (101 MHz, CDCl₃): δ 150.3, 148.0, 142.4, 136.9, 128.9, 127.4, 121.6, 28.7 ppm.

1.2. Characterization techniques

1.2.1. Grazing Incidence Small Angle X-Ray Scattering (GIWAXS) Experiments

GIWAXS measurements of the synthesized samples prepared under different stoichiometric conditions were performed at the Austrian SAXS beamline at ELETTRA, Trieste. An X-ray beam with a wavelength of 1.54 Å (beam energy 8 keV) was used with a sample-to-detector distance of 260 mm, providing a q -range of $0.01 < q < 29.21 \text{ nm}^{-1}$, where q denotes the magnitude of the scattering vector. The beam size was $0.1 \times 1 \text{ mm}$ ($v \times h$). The angular scale of the detector was calibrated using silver behenate. Samples were mounted on a motorized stage with a resolution of 0.001° , and the incident grazing angle was set to 1.6° .

The 2D GIWAXS patterns were acquired in triplicate with an exposure time of 30 s each. A Pilatus3 1M detector (Dectris Ltd., Baden, Switzerland; active area $169 \times 179 \text{ mm}^2$, pixel size $172 \text{ }\mu\text{m}$) was used, and the detector images were processed using SAXSDOG, a software developed at the Austrian SAXS beamline for automatic data reduction.[¹] For data analysis, radially integrated diffraction patterns were considered. The integrated data were further processed using IGOR Pro (Wavemetrics, Inc., Lake Oswego, OR). Crystalline phases were identified by indexing the relative positions of the Bragg peaks in the scattering patterns and comparing them with bulk diffraction patterns of the well-known single-crystal DMOF structure (Figure S6).[²]

1.2.2. IR spectromicroscopy

Infrared (IR) measurements were performed at the SISSI-Bio offline end station of the SISSI beamline at Elettra Sincrotrone Trieste. The IR spectromicroscopy setup is equipped with a grazing-angle objective (GAO), which is essential for the analysis of ultrathin films supported on metallic or highly reflective substrates. Spectra were acquired in slow acquisition mode by averaging 128 scans at a spectral resolution of 2 cm^{-1} and a scanner speed of 60 kHz. The apertures were set to $75 \times 75 \text{ }\mu\text{m}^2$ to achieve an optimal signal-to-noise ratio and enable detection of subtle spectral variations. A broadband mercury cadmium telluride detector (MCT-B), operating in the $3800\text{--}400 \text{ cm}^{-1}$ spectral range, was used for signal detection.

1.2.3. SEM and EDS measurements

Morphologies of samples were observed by using a focused ion beam–scanning electron microscope (FIB–SEM; Aquilos2, Thermo Fisher Scientific, The Netherlands)

and cross-sectional analyses were carried out using a focused ion beam–scanning electron microscope (FIB–SEM; Helios G5 UC, Thermo Fisher Scientific, The Netherlands) equipped with a multi gas injection system (GIS) and an Ultim Max 65 energy-dispersive X-ray spectroscopy (EDS) detector (Oxford Instruments, UK). Prior to analysis, the samples were sputter-coated with a 6 nm platinum (Pt) layer using a PECS 682 system (Gatan, USA) to minimize surface charging.

1.2.4. ToF-SIMS measurements

Time-of-flight secondary ion mass spectrometry (ToF-SIMS) measurements were performed using a M6 instrument (IONTOF GmbH, Münster, Germany) equipped with a bismuth liquid metal ion gun (LMIG) for analysis and an argon gas cluster ion beam (GCIB) for sputtering. Measurements were conducted in negative ion mode. For spectral acquisition and imaging, a pulsed Bi_3^+ primary ion beam was employed as the analysis source. Depth profiling experiments were carried out using an Ar_{2000}^+ GCIB operated at an acceleration energy of 2.5 keV and a sputter current of 1 nA. The sputter beam was rastered over a larger area of 500 μm by 500 μm , while secondary ions were collected only from the central analysis region over an area of 300 μm by 300 μm (128 by 128 pixels) to avoid contributions from crater edges. Analysis and sputtering were alternated in a cyclic manner to obtain depth-resolved chemical information. High lateral resolution two-dimensional chemical imaging was performed using the delayed extraction analyzer mode in combination with the fast imaging LMIG mode. Imaging was conducted over a field of view of 52 μm by 52 μm (512 by 512 pixels). Charge compensation was applied during all measurements using a low-energy electron flood gun (20 eV). Mass calibration was performed using the signals for C_3^- at mass-to-charge (m/z) 36.00, C_4^- at m/z 48.00, and C_5^- at m/z 60.00. All data acquisition, visualization, and post-processing were carried out using SurfaceLab 7.6 software (IONTOF GmbH).

Two-dimensional ToF-SIMS images were acquired using the delayed extraction mode combined with fast imaging LMIG mode, with results shown in Figure 4 d. This approach provides high mass resolution ($\sim 10,000$) while maintaining lateral resolution of ~ 100 nm. The ZnOH^- signal is homogeneously distributed across the scanned area, reflecting the presence of Zn–O(H) species within the film. The formation of $\text{Zn}(\text{OH})_2$ is unlikely, as its characteristic signals would produce clear features in the IR spectrum of the fabricated films, which were not observed (at 3300 cm^{-1}). Therefore, the ZnOH^- signal is more likely generated from ZnO via hydrogen attachment during Bi_3^+

bombardment or post-ionization processes and should be considered a marker of Zn–O(H) species rather than a unique identifier of a single phase.

2. LPE Spin-Coating Workflow

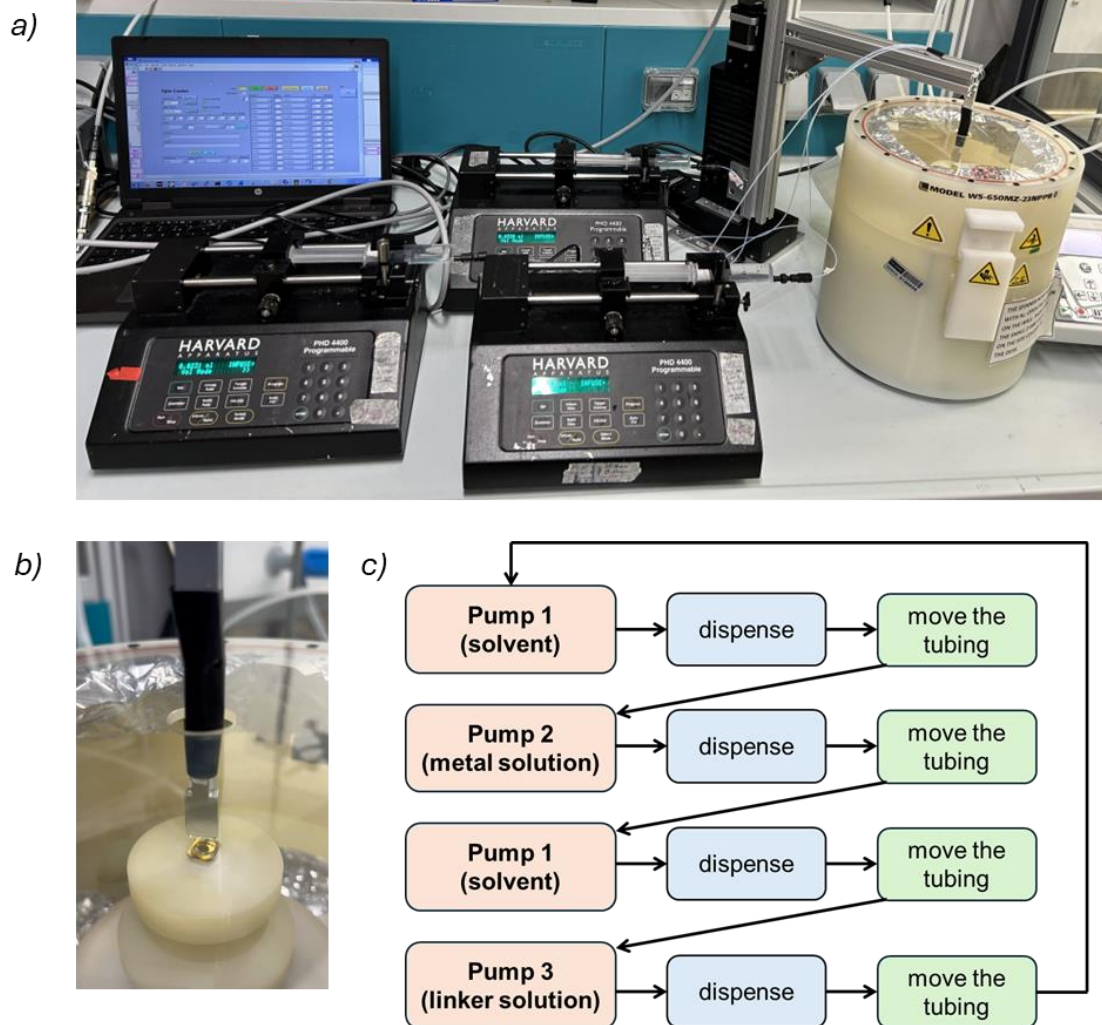


Figure S1. Process overview of the automatic deposition step. (a) Photograph of the LbL LPE spin-coating setup; (b) tube holder that moves according to the programmed sequence to precisely dispense the solution at the center of the wafer. (c) Programmed sequence of steps representing one deposition cycle.

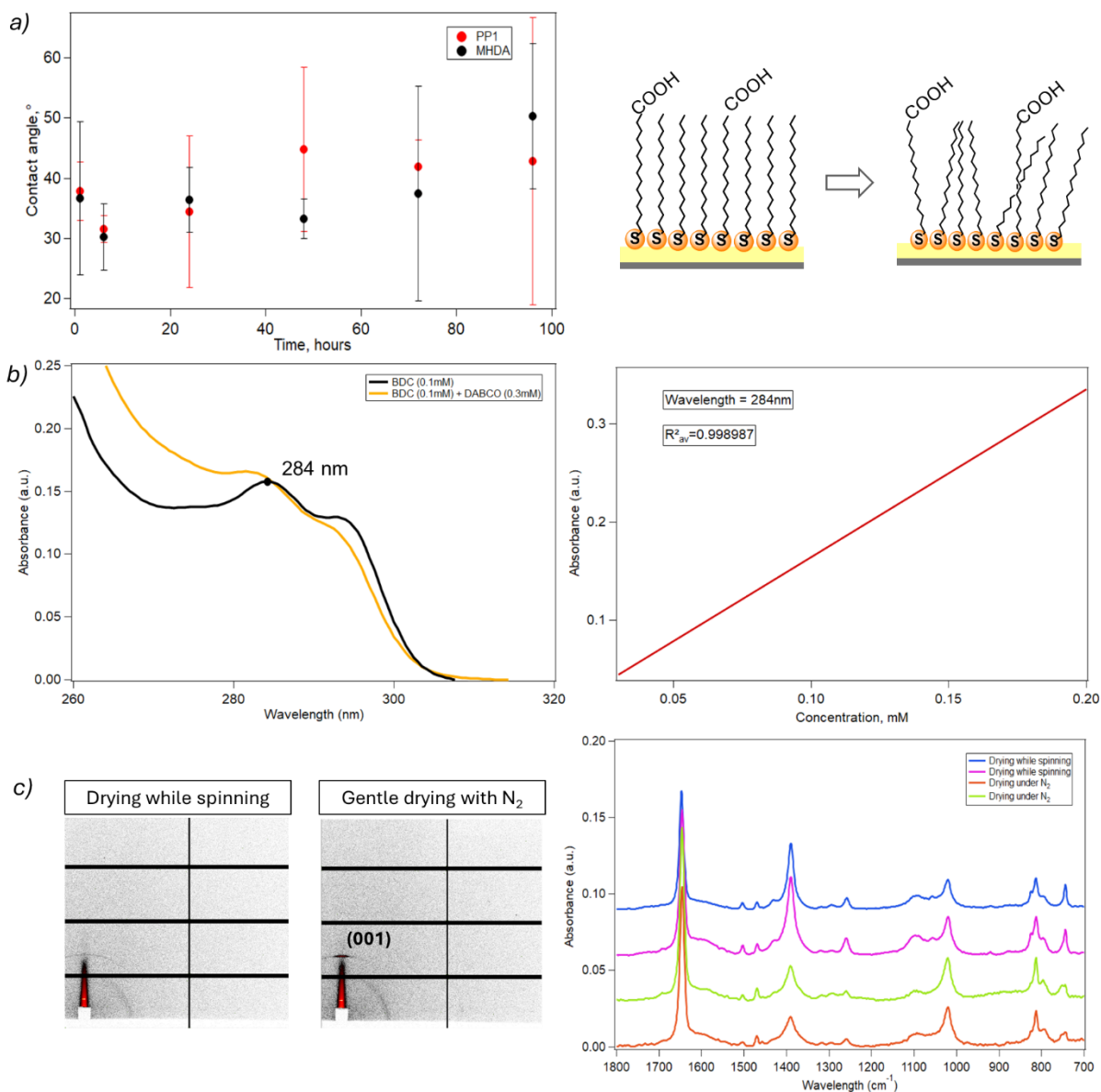
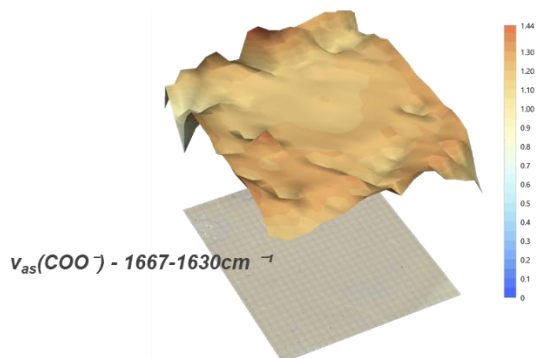


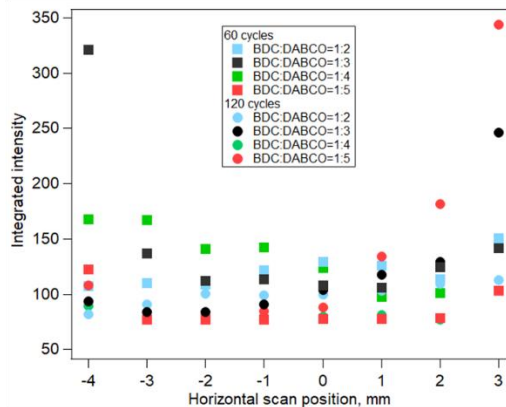
Figure S2. (a) Contact angle measurements showing a progressive loss of order in the SAM layer within time. Each data point represents the average of three independent samples, and the error bands indicate the presence of structural variability even under optimal functionalization conditions.^[3] However, the present study demonstrates that using functionalized substrates within the first 48h enables reproducible growth of highly oriented and homogeneous MOF films. (b) UV-Vis absorption spectra of a 0.1 mM BDC solution and the calibration curve at the wavelength of interest. (c) GIWAXS 2D patterns (left) of duplicates, illustrating the loss of crystallinity when the sample is allowed to dry during spinning. The IR spectra (right) confirm that chemical composition of the MOF remains unchanged irrespective of drying method.

3. Assessment of film uniformity and fabrication reproducibility

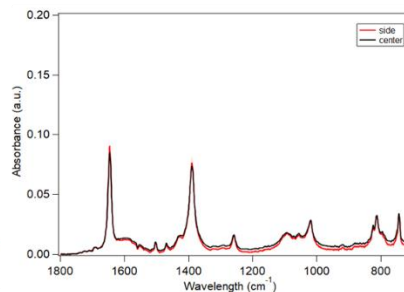
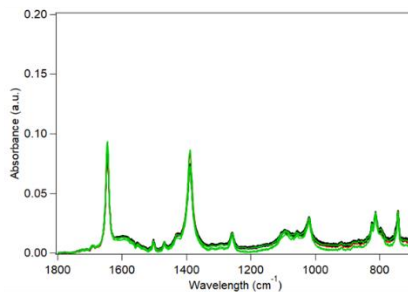
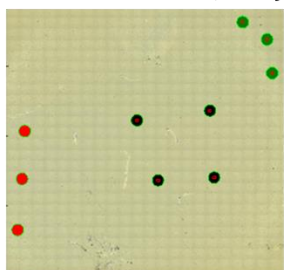
a) BDC:DABCO = 1:3, 60 cycles



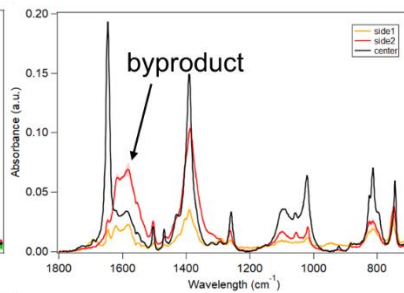
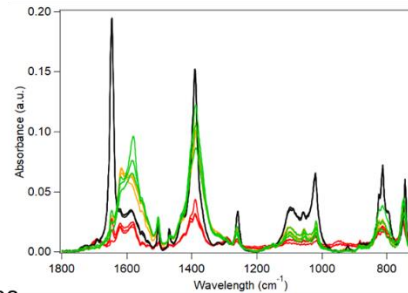
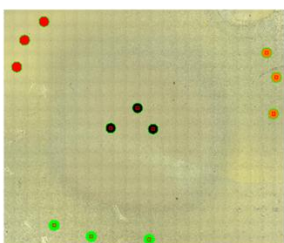
b)



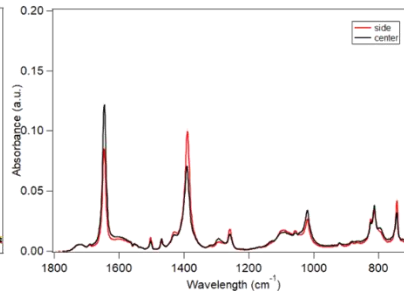
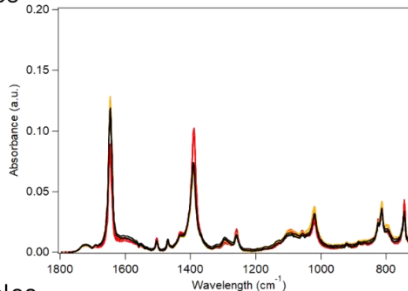
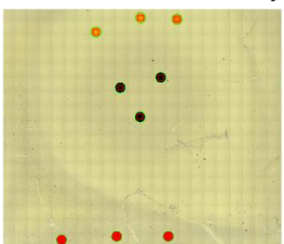
c) BDC:DABCO = 1:2, 60 cycles



BDC:DABCO = 1:2, 120 cycles



BDC:DABCO = 1:5, 60 cycles



BDC:DABCO = 1:5, 120 cycles

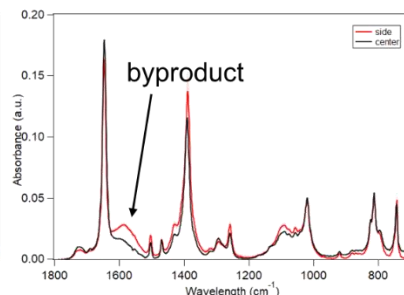
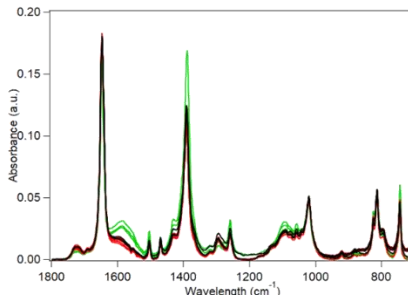
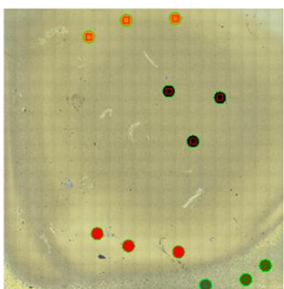


Figure S3. IR and GIWAXS uniformity analysis (a) 3d-projection of the $\nu_{\text{as}}(\text{COO}^-)$ intensity in the range of $1667\text{-}1630\text{cm}^{-1}$ over the all sample area (BDC : DABCO= 1 : 3) with 60 cycles, indicating formation of MOF. (b) GIWAXS measurements across the sample, where 0 mm is position in the centre of wafer: integrated out-of-plane intensity versus horizontal position that confirmed higher uniformity of the 60 cycles samples. (c) IR-data for the samples with BDC:DABCO=1:2/1:5 molar ratios with 60/120. Each wafer was first imaged and subsequently probed at 3-4 different locations (center and edges) to compare spectral features across distinct surface regions. Colour of the spectra in the central column corresponds to the colour of the point in the image. For each location, the collected spectra were averaged and plotted with corresponding error bars. Samples prepared with 60 deposition cycles and varying reagent molar ratios exhibit high uniformity across the entire wafer, including the edges. In contrast, increasing the number of cycles to 120 results in a loss of homogeneity and the appearance of by products at the wafer edges.

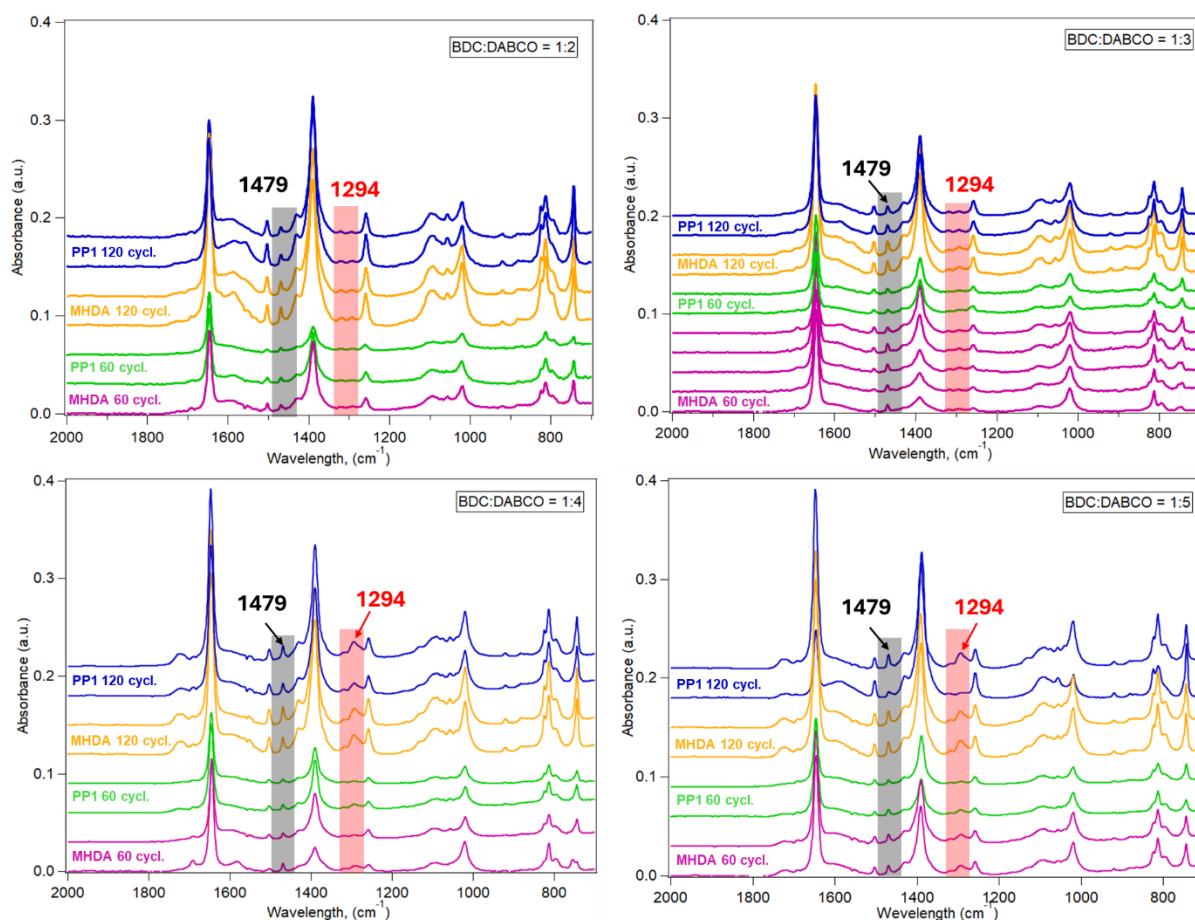


Figure S4. IR spectra of samples prepared with varying BDC:DABCO molar ratios and deposition cycles confirm the reproducibility of the LbL-LPE spin-coating method. The

band at 1294 cm^{-1} , assigned to unreacted DABCO, appears only in the 1:5 samples and in the 1:4 samples after 120 cycles due to increased material deposition. In contrast, the band at 1479 cm^{-1} corresponds to coordinated DABCO and is weak in the samples synthesized with a 1:2 ligand ratio, 60 cycles.

4. DFT calculations

To reproduce the experimental spectrum as best as possible to be able to accurately assign the bands to their vibrational modes, DFT calculations were performed.

4.1. Computational Details

The initial model structures of $\text{Zn}_2\text{BDC}_2\text{DABCO}$ were generated based on the computational structures of Griffith et al.^[4] using VESTA and the GUI of the atomic simulation environment (ASE) to yield a $\sqrt{2} \times \sqrt{2} \times 1$ supercell.^[5]

DFT calculations were performed with FHI-aims^[6-11] (version 210716_2) employing light settings^[6] and the PBE functional^[12] with the many-body dispersion correction^[13,14] (PBE+MBD/light). Relativistic effects were treated by the scalar atomic ZORA approximation as implemented in FHI-aims. The k-grids for both the periodic DFT calculations and the MBD energies and forces were set to always satisfy $nq > 30\text{ \AA}$, with q being the cell length in the respective direction and n being the number of k-points in that direction. Convergence criteria were set to 10^{-6} eV for the energy, 10^{-4} eV/\AA for the gradient, 10^{-3} for the sum of eigenvalues and 10^{-5} for the density.

Optimizations with fixed cell parameters were performed with the FHI-AIMS implementation of the BFGS optimizer with an energy tolerance of 0.001 eV and enforcing a maximum force of 0.005 eV/\AA (Figure SI1 to SI3).

Full cell optimizations were performed by employing the BFGS implementation and ExpCellFilter class of ASE,^[6] enforcing a maximum force of 0.005 eV/\AA .

Vibrational spectra were calculated by the finite displacement approach as implemented in Phonopy.^[15,16] The respective calculations were performed on the same $\sqrt{2} \times \sqrt{2} \times 1$ supercells with finite displacements of 0.005 \AA . The optimized geometries were checked to not exhibit any imaginary modes at the Γ -point. Born effective charges were calculated via a finite differences approach using the BEC.py script of FHI-aims (displacements were chosen to be 0 and 0.005 \AA and the polarization k-grid along the reciprocal lattice vectors was set to $k_x = 8 \times 2 \times 2$, $k_y = 2 \times 8 \times 2$ and $k_z = 2 \times 2 \times 8$). The dielectric tensors were calculated with Density-functional

perturbation theory (DFPT), retaining all other relevant settings. Infrared spectra at the individual volumes were obtained via the Phonopy-Spectroscopy code.^[17,18]

Animation files for the Phonon modes were generated with Phonopy and visualized with Jmol. ^[15,16,19] Similarly, the geometries depicted below were rendered in Jmol.

4.2. Detailed Information on the Computations

Firstly, full cell optimizations of Zn₂BDC₂DABCO were performed for five different model structures (**I** to **V**). The resulting geometries (Figures S5 to S7) exhibit only subtle structural differences, especially regarding DABCO orientation and the arrangement of the coordination sphere metal nodes (the resulting cell parameters are summarized in Table S2). The obtained volumes are in good agreement with the experimental X-ray structure (with deviations around 0.6%, see Table S1) and the electronic energies of the structures differ only marginally and are within the error of the method (the maximum absolute deviation is 2.28×10^{-3} eV or 0.22 kJ/mol). Gratifyingly, the obtained IR-spectra display almost no dependence on the structural model used, as they are visually virtually indistinguishable (Figures S10).

Secondly, an alternative way to obtain calculated IR spectra that accurately reflect the experimental data and, thus, allow reliable assignment of the individual bands, is to fix the cell parameters to their experimentally determined values. Hence, in addition to the above outlined full cell optimization approach we also opted to pursue this strategy to assess the robustness of our calculated IR spectra and their dependence on the chosen computational model. Towards this, all model structures **I** to **V** were also optimized with the cell parameters fixed to the experimentally determined values (termed **I-exp.** to **V-exp.**).^[4] Of the five structures, only **I-exp.** and **V-exp.** did not exhibit an imaginary frequency at the Γ -point. Their geometries are displayed and compared to their respective parent structures **I** and **V** in Figures S8 and S9. Importantly, the IR-spectra obtained for **I-exp.** and **V-exp.** only slightly differ from the ones obtained from the fully optimized model structures **I** to **V** (Figures S5- S7), rendering the qualitative conclusions obtained independent of the chosen computational approach, i.e., full cell optimization versus internal cell optimization with cell parameters fixed to their experimental values. This also applies to the peak assignment, see section 5, Table S3. For the main text of the publication, the IR-spectrum obtained from model structure **V-exp.** was chosen.

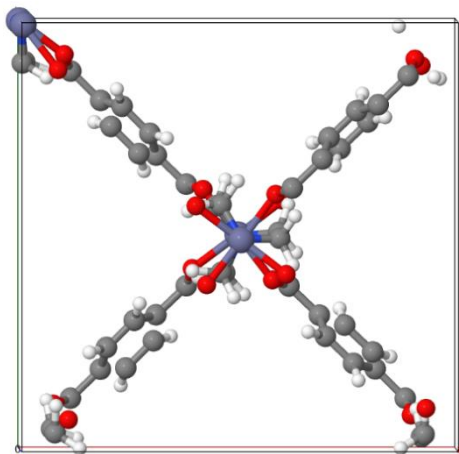
Table 1. Cell volumes and electronic energies of the calculated model structures and comparison to the experiment (entry “Exp.”).

structure	V [Å ³]	E [eV]	ΔE [eV]	ΔE vs. I [kJ/mol]	ΔV vs exp. [Å ³]	ΔV vs exp. [%]
I	2308.236	-281489.208635371	0.00	0.00	13.438	0.59
II	2309.324	-281489.208479918	1.04×10 ⁻⁴	0.01	14.526	0.63
III	2310.473	-281489.207031581	1.55×10 ⁻³	0.15	15.676	0.68
IV	2310.421	-281489.206387599	2.28×10 ⁻³	0.22	15.624	0.68
V	2310.590	-281489.207266224	1.35×10 ⁻³	0.13	15.792	0.69
I-exp.	2294.797	-281489.149519445	5.91×10 ⁻²	5.70	0.000	0.00
V-exp.	2294.797	-281489.150958683	5.77×10 ⁻²	5.57	0.000	0.00
Exp.	2294.797	n.a.	n.a.	n.a.	0.000	0.00

Table 2. Cell parameters of the calculated model structures and comparison to the experiment (entry “Exp.”).

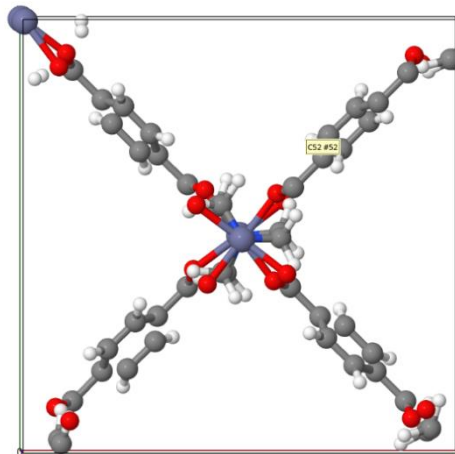
structure	a [Å]	b [Å]	c [Å]	α [°]	β [°]	γ [°]
I	15.724	15.419	9.523	91.057	89.123	90.010
II	15.610	15.534	9.524	90.490	89.358	89.999
III	15.581	15.565	9.527	89.714	89.896	89.997
IV	15.634	15.514	9.526	90.203	89.781	90.006
V	15.595	15.551	9.527	89.761	89.853	89.998
I-exp.	15.455	15.455	9.608	90.000	90.000	90.000
V-exp.	15.455	15.455	9.608	90.000	90.000	90.000
Exp.	15.455	15.455	9.608	90.000	90.000	90.000

P 1 [P 1] #1
a=15.724Å
b=15.419Å
c=9.523Å
α=91.057°
β=89.123°
γ=90.010°



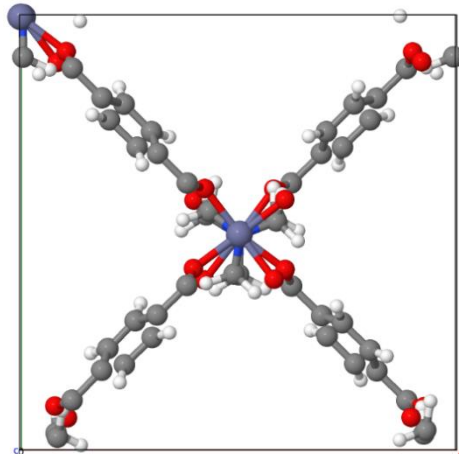
I

P 1 [P 1] #1
a=15.818Å
b=15.534Å
c=9.524Å
α=90.490°
β=89.358°
γ=89.999°



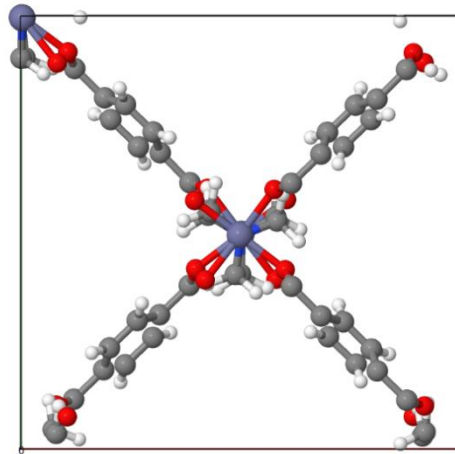
II

P 1 [P 1] #1
a=15.381Å
b=15.565Å
c=9.527Å
α=89.714°
β=89.896°
γ=89.997°



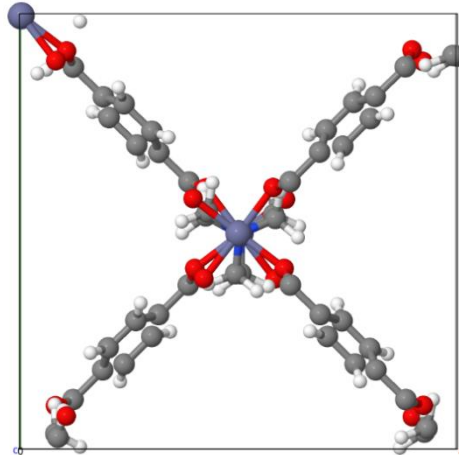
III

P 1 [P 1] #1
a=15.828Å
b=15.514Å
c=9.526Å
α=90.203°
β=89.781°
γ=89.006°



IV

P 1 [P 1] #1
a=15.595Å
b=15.551Å
c=9.527Å
α=89.781°
β=89.853°
γ=89.998°



V

Figure S5. Rendered images of the 3D structures of models I to V (view along the z-axis).

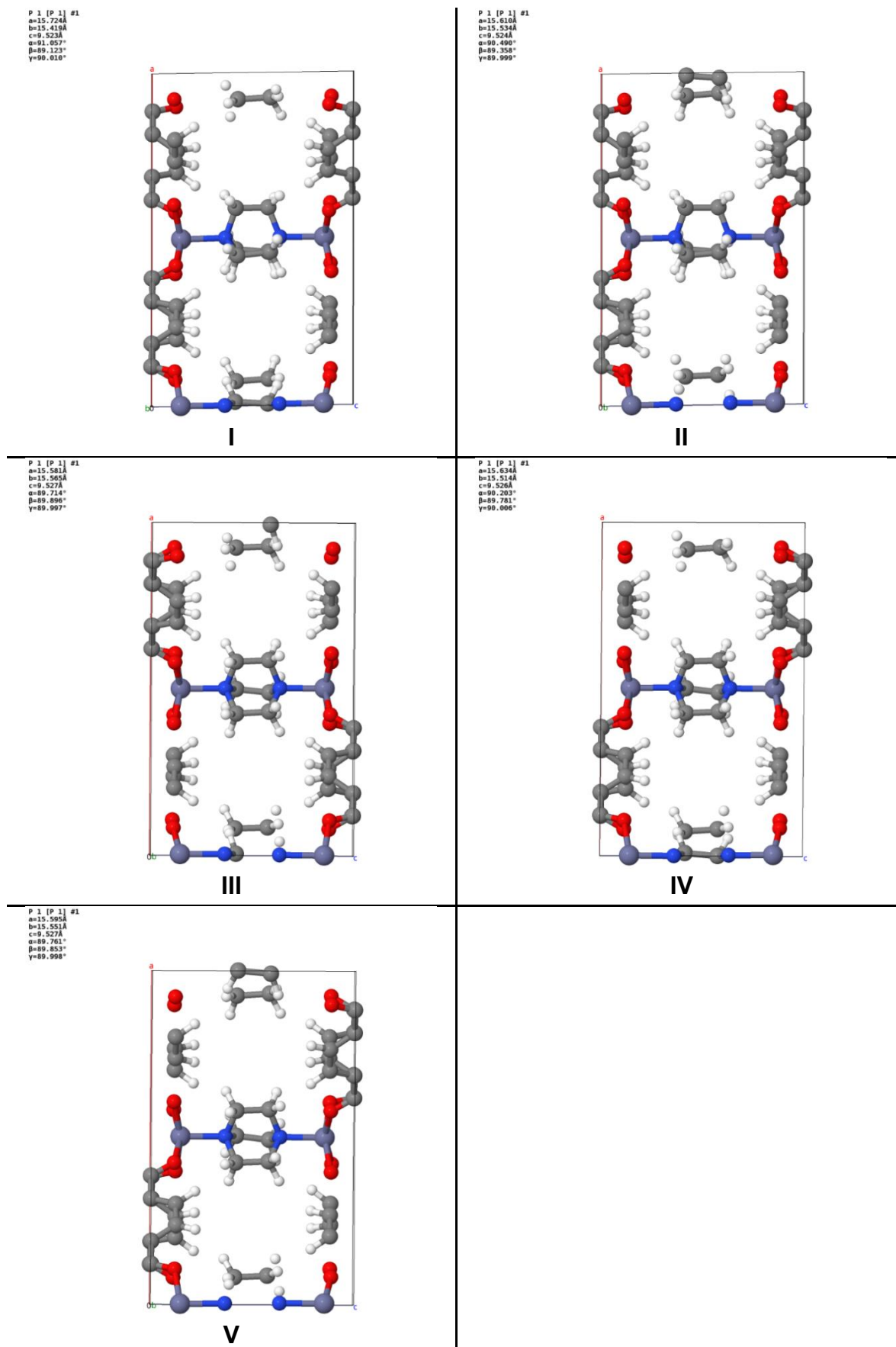
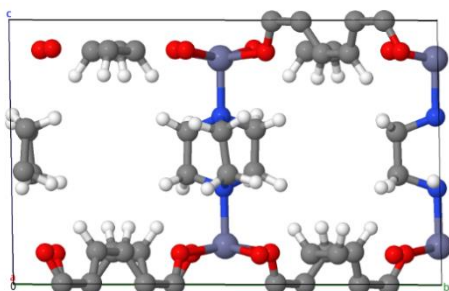


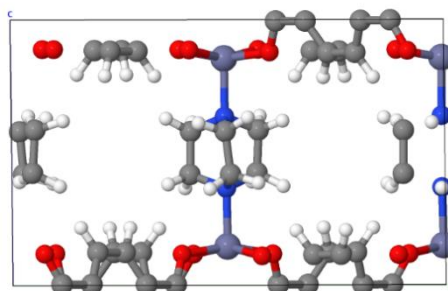
Figure S6. Rendered images of the 3D structures of models I to V (view along the y-axis).

P 1 [P 1] #1
a=15.724
b=15.419Å
c=9.523Å
α=91.057°
β=89.123°
γ=90.018°



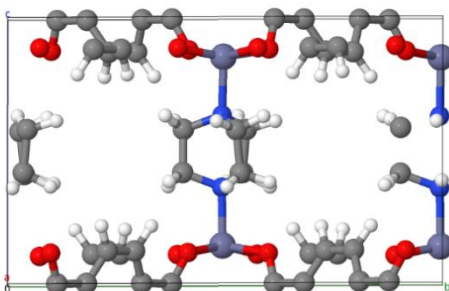
I

P 1 [P 1] #1
a=15.616Å
b=15.534Å
c=9.524Å
α=90.490°
β=89.358°
γ=89.999°



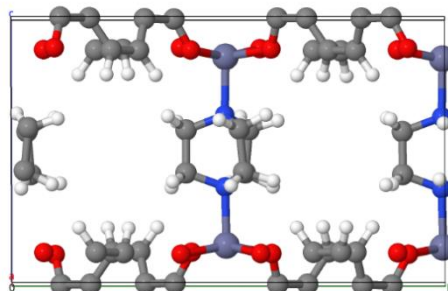
II

P 1 [P 1] #1
a=15.581Å
b=15.565Å
c=9.527Å
α=89.714°
β=89.898°
γ=89.997°



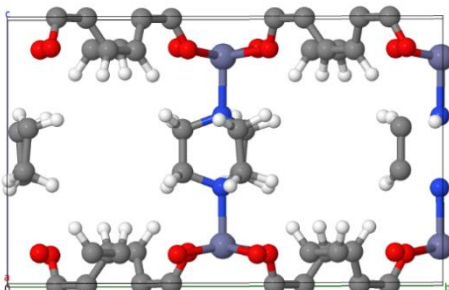
III

P 1 [P 1] #1
a=15.634Å
b=15.514Å
c=9.526Å
α=90.203°
β=89.781°
γ=89.006°



IV

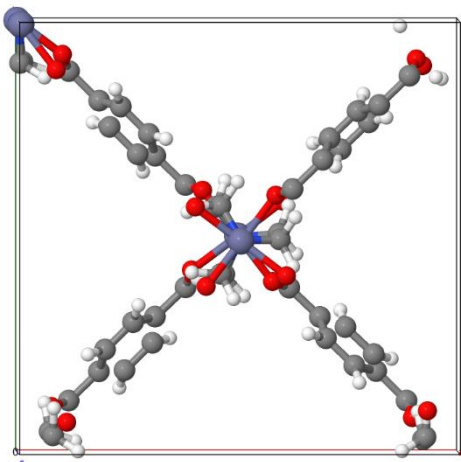
P 1 [P 1] #1
a=15.595Å
b=15.551Å
c=9.527Å
α=89.761°
β=89.853°
γ=89.998°



V

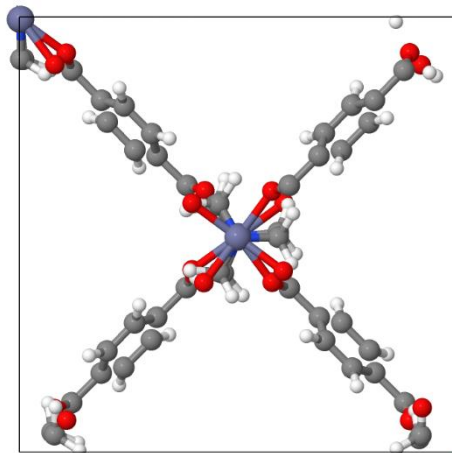
Figure S7. Rendered images of the 3D structures of models I to V (view along the x-axis).

P 1 [P 1] #1
a=15.724Å
b=15.419Å
c=9.523Å
α=91.057°
β=89.123°
γ=90.010°



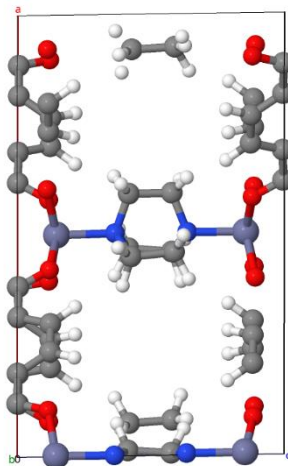
I

P 1 [P 1] #1
a=15.456Å
b=15.456Å
c=9.608Å
α=90.000°
β=90.000°
γ=90.000°



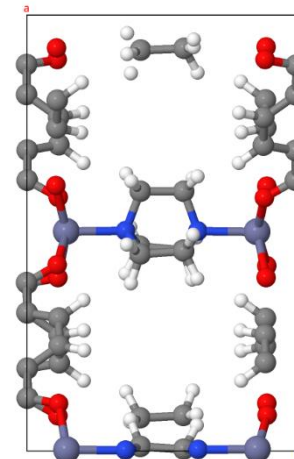
I-exp.

P 1 [P 1] #1
a=15.724Å
b=15.419Å
c=9.523Å
α=91.057°
β=89.123°
γ=90.010°



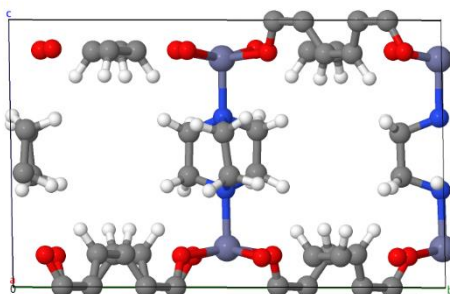
I

P 1 [P 1] #1
a=15.456Å
b=15.456Å
c=9.608Å
α=90.000°
β=90.000°
γ=90.000°



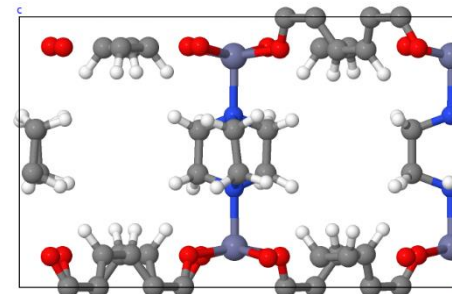
I-exp.

P 1 [P 1] #1
a=15.724Å
b=15.419Å
c=9.523Å
α=91.057°
β=89.123°
γ=90.010°



I

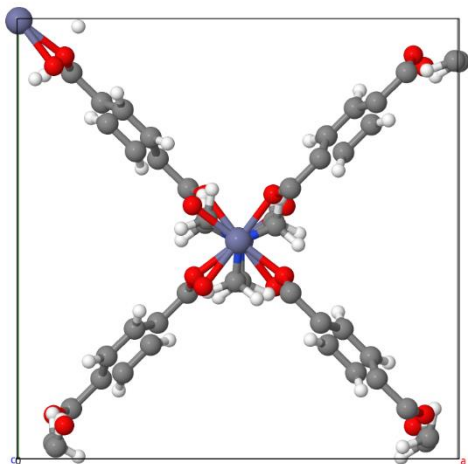
P 1 [P 1] #1
a=15.456Å
b=15.456Å
c=9.608Å
α=90.000°
β=90.000°
γ=90.000°



I-exp.

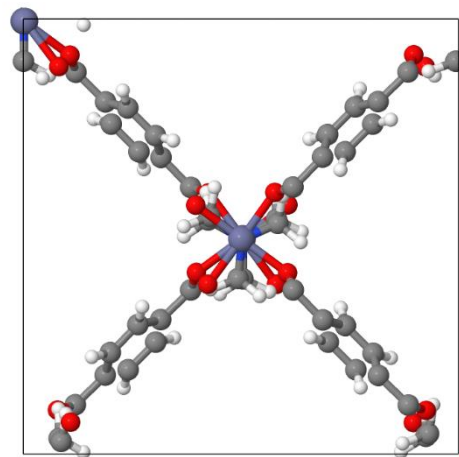
Figure S8. Comparison of the 3D structures of **I** (left) and **I-exp.** (right).

P 1 [P 1] #1
a=15.595Å
b=15.551Å
c=9.527Å
α=89.761°
β=89.853°
γ=89.998°



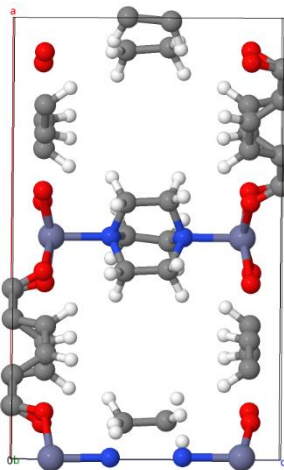
V

P 1 [P 1] #1
a=15.456Å
b=15.456Å
c=9.608Å
α=90.000°
β=90.000°
γ=90.000°



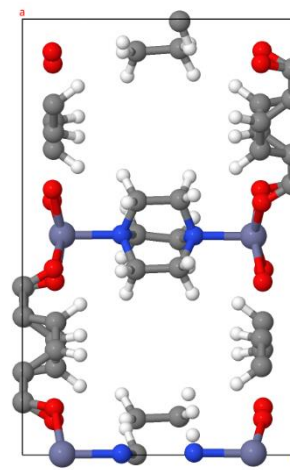
V-exp.

P 1 [P 1] #1
a=15.595Å
b=15.551Å
c=9.527Å
α=89.761°
β=89.853°
γ=89.998°



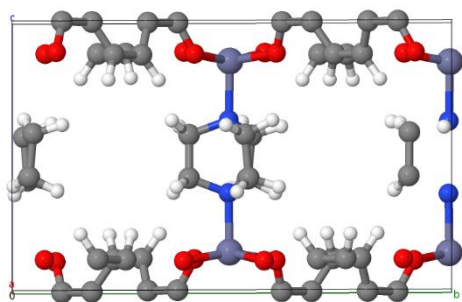
V

P 1 [P 1] #1
a=15.456Å
b=15.456Å
c=9.608Å
α=90.000°
β=90.000°
γ=90.000°



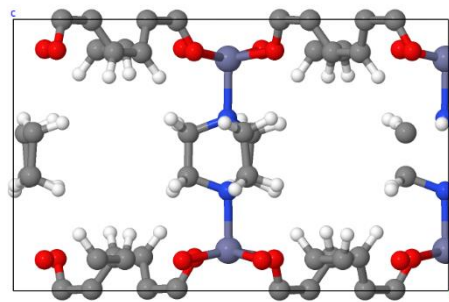
V-exp.

P 1 [P 1] #1
a=15.595Å
b=15.551Å
c=9.527Å
α=89.761°
β=89.853°
γ=89.998°



V

P 1 [P 1] #1
a=15.456Å
b=15.456Å
c=9.608Å
α=90.000°
β=90.000°
γ=90.000°



V-exp.

Figure S9. Comparison of the 3D structures of **V** (left) and **V-exp.** (right).

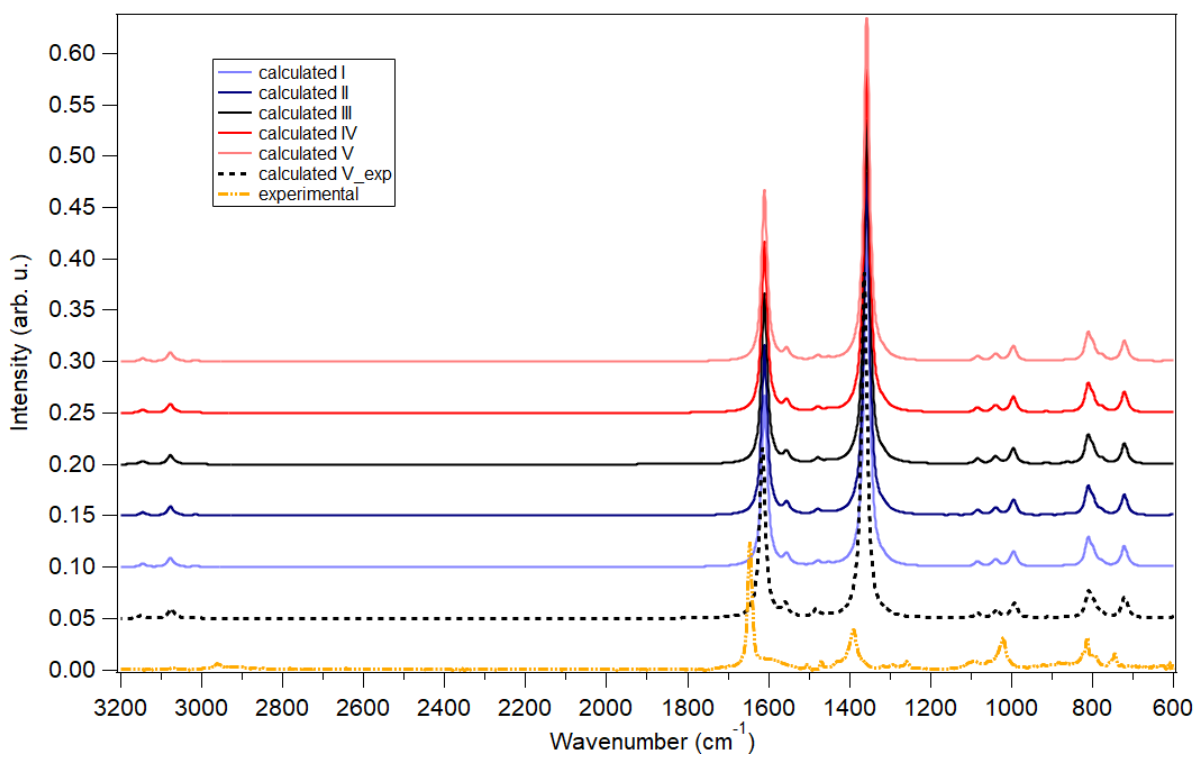


Figure S10. Overlay of the calculated IR-Spectra for the investigated model structure.

5. Calculated vs. experimental IR spectra and vibrational peaks assignment

To compare the two computational model approaches and obtain a conclusion that is qualitatively independent of the chosen model, the assignment of the peaks was done on structures **IV** and **V-exp.**, representative of the two above outlined computational model approaches, i.e., full cell optimization versus internal cell optimization with cell parameters fixed to their experimental values. The computational spectra of **IV** and **V-exp.** both well reflect the experimental spectrum (Figure S11). The individual bands in the experimental spectrum were assigned to the respective type of mode by selecting the most intense individual vibrations making up the corresponding bands in the theoretical spectra of **IV** and **V-exp.**, subsequent visual inspection in the animation file and, where possible, compared to literature.^[20–22] Gratifyingly, the assignment of the peaks does not differ between **IV** and **V-exp.**, rendering the obtained picture independent of the computational model approach.

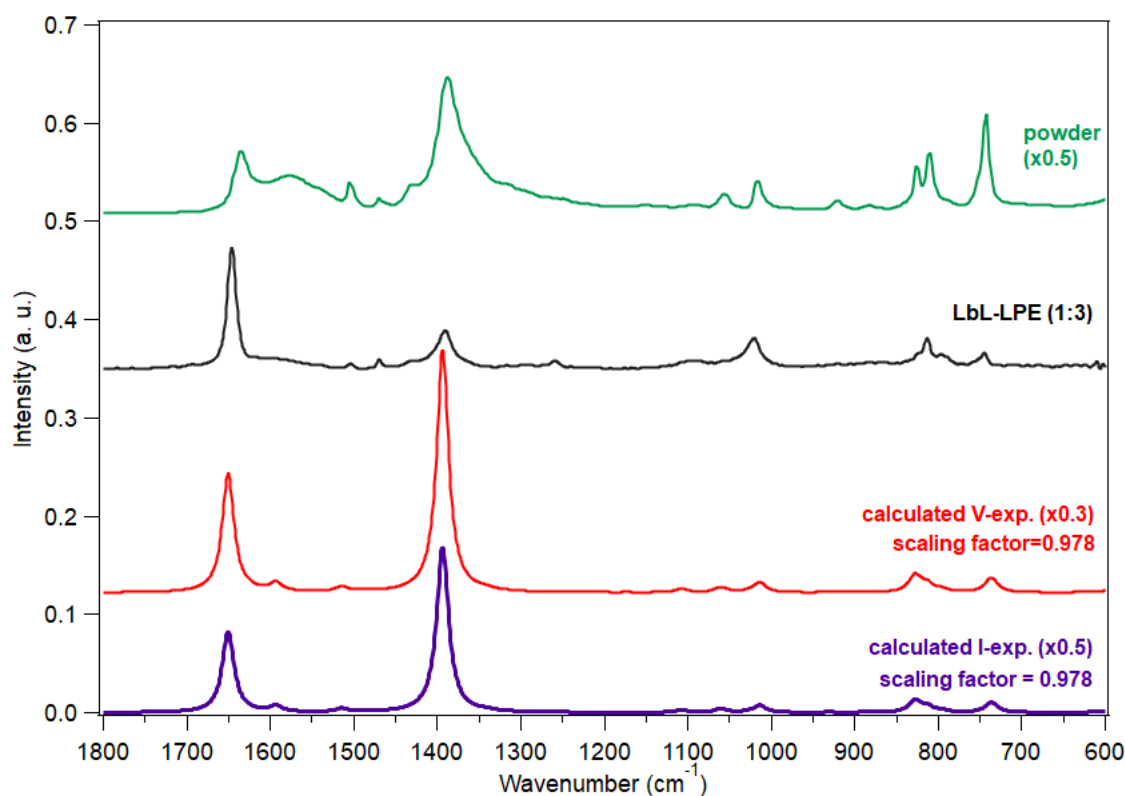


Figure S11. Comparison of calculated structures **IV** and **V-exp.** with the experimental spectra of the LbL-LPE film (optimal conditions) and the bulk powder. The calculated spectrum matches the bulk powder spectrum, while the oriented structure has a different intensity distribution between asymmetric and symmetric carboxylic group vibrations. This is known to occur for oriented structures, as shown for SSH-fabricated $\text{Cu}_2\text{BDC}_2\text{DABCO}$ films by Baumgartner et al.^[23] The calculated IR spectrum was

scaled (≈ 0.9) along the frequency axis to correct for the systematic overestimation of vibrational frequencies inherent to the harmonic approximation used in theoretical calculations, enabling better agreement with the experimental spectrum.^[24]

Table S3. Assignment of the vibrational bands in the calculated and experimental spectra.

Frequency in experimental spectrum, cm^{-1}	Frequency in calculated spectrum IV, cm^{-1}	Frequency in calculated spectrum V-exp., cm^{-1}	Vibrations
1646	1610	1615	COO ⁻ stretching asymmetric
1588	1555	1559	BDC stretching asymmetric
1479	1478	1480	DABCO CH ₂ bending
1391	1358	1363	BDC stretching symmetric
			COO ⁻ stretching symmetric
			DABCO NC ₃ stretching symmetric CH ₂ bending
1092	1083	1085	BDC C-H scissoring
1021	1038	1037	DABCO C-C stretching asymmetric
1022	995	992	DABCO NC ₃ scissoring
812	810	810	DABCO C-C stretching symmetric
744	721	718	BDC C-H wagging

6. GIWAXS Characterization of $\text{Zn}_2(\text{BDC})_2(\text{DABCO})$ Films

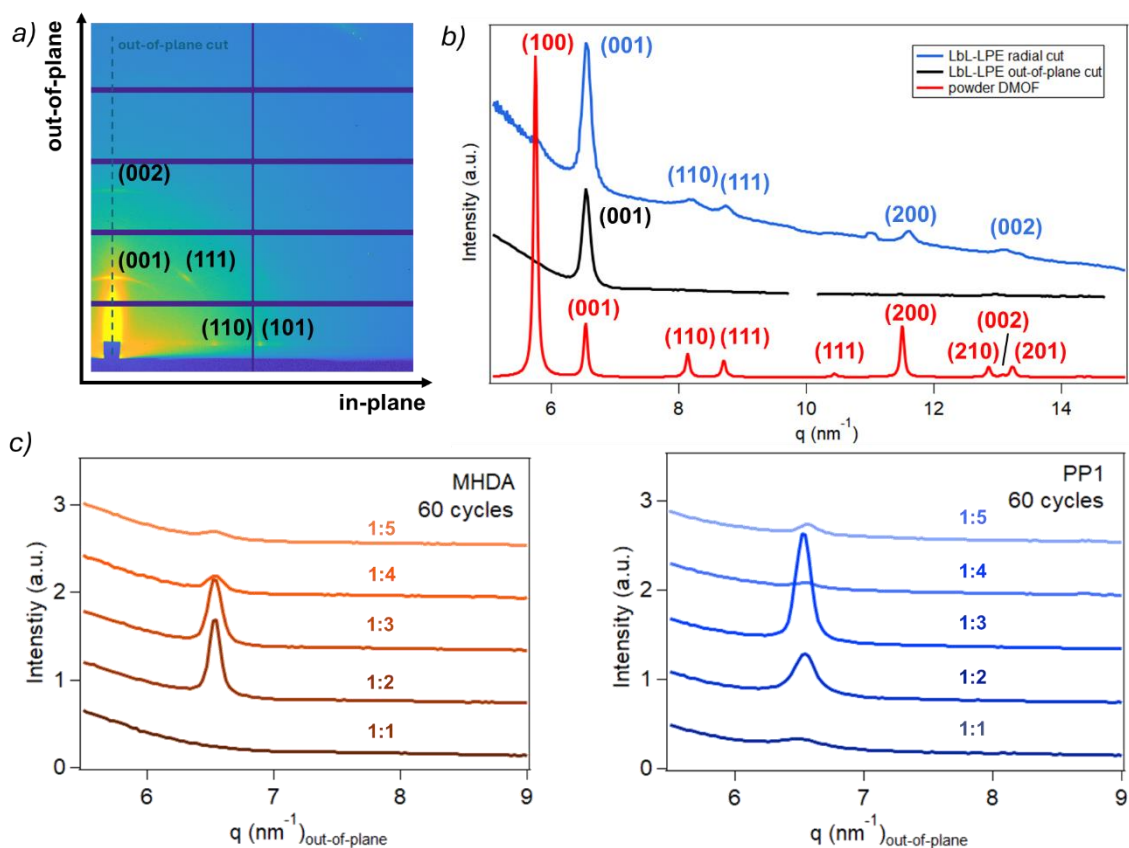


Figure S12. Crystalline phase identification and homogeneity of the films. (a) Radial integration of the 2D detector pattern. The cut margin for the out-of-plane integration was set to 10 pixels. (b) Comparison with the powder diffraction pattern of the sample prepared under optimal conditions confirms that the dominant reflection corresponds to the (001)-oriented MOF phase. The presence of the (110), (111), and (101) reflections is related to the presence of tilted crystallites. (c) Out-of-plane integration of the GIWAXS intensity of MOF thin films with different molar ratios on the MHDA and PP1 functionalized SAM layers.

7. Surface and cross-section morphology

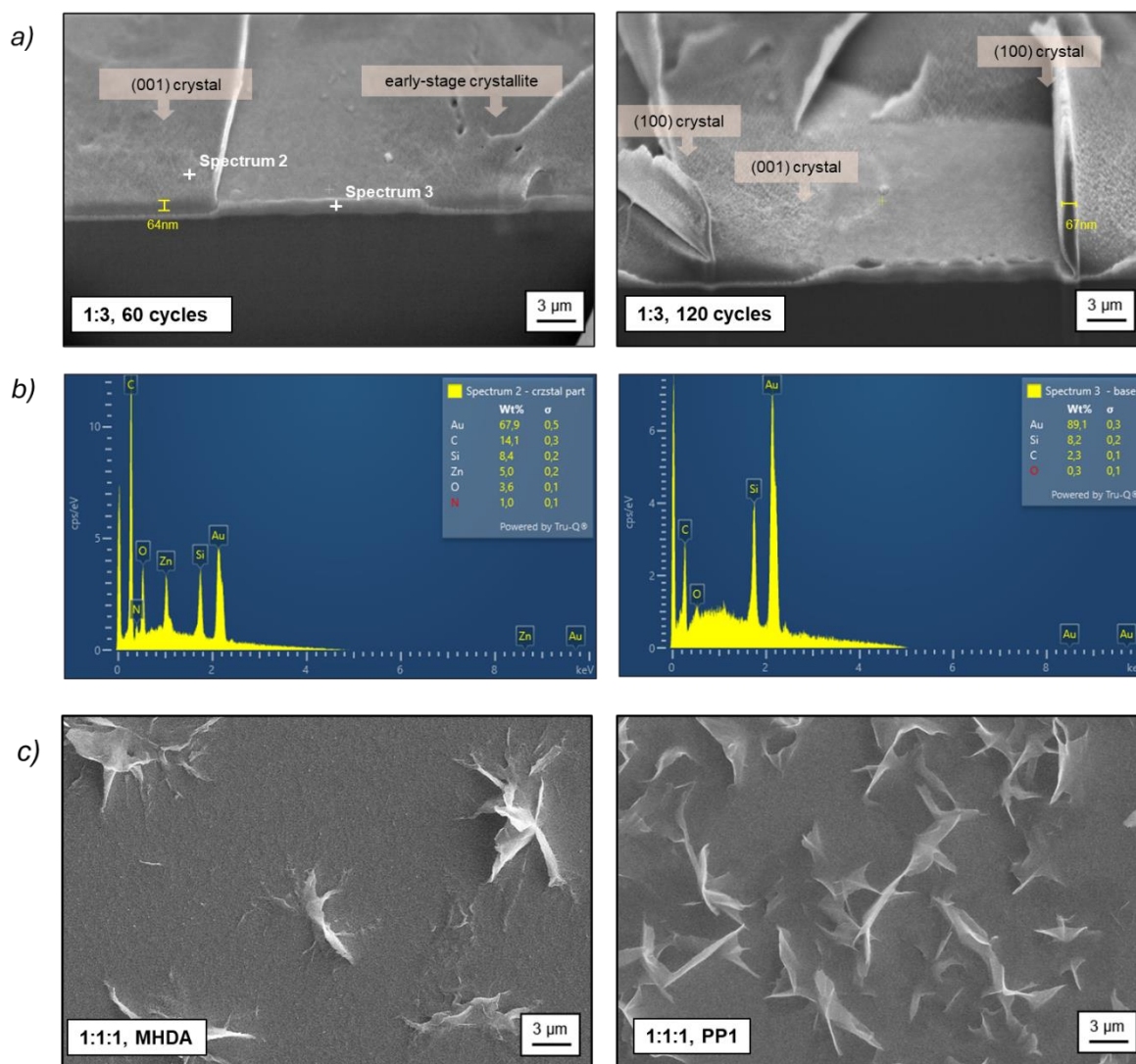


Figure S13. SEM and EDS Analysis of MOF Film Morphology. (a) SEM images of FIB-cut samples of 60 and 120 synthesis cycles with the molar ratio Zn:BDC:DABCO = 1:1:3. (b) EDS spectra collected from two regions of the film surface: on a crystal (Spectrum 2) and in the area between crystals (Spectrum 3). The EDS data indicate that the regions between the crystals contain no metal, suggesting that MOF growth follows an island-like mechanism. (c) SEM images of the non-crystalline samples with the molar ratio Zn:BDC:DABCO=1:1:1.

8. Thin film thickness measurement with 3D profilometry

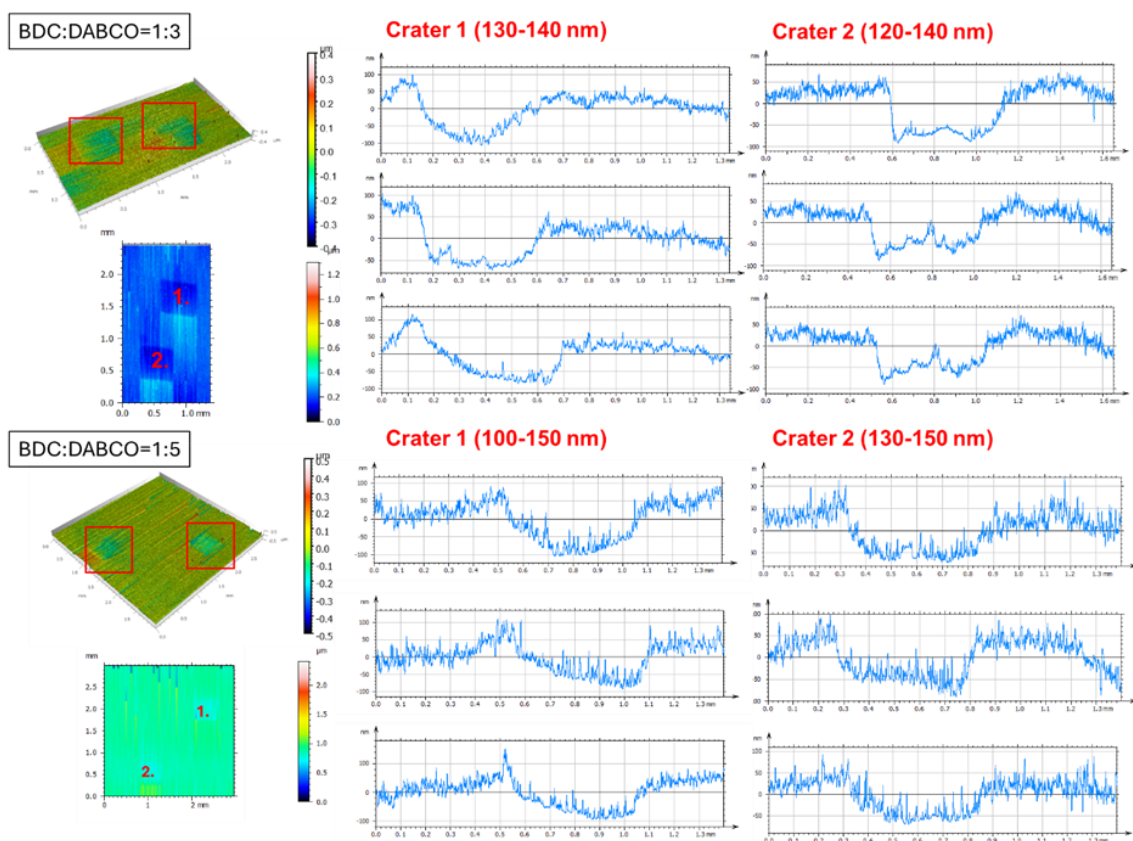


Figure S14. Sample Thickness Determination. Determination of the thickness of samples with 1:3 and 1:5 BDC:DABCO ligand ratios by creating two craters on each sample using ToF-SIMS and GCIB sputtering, and subsequently measuring height differences across a surface using 3D profilometry. Results confirm the total film thickness, which consists of ~70nm of crystal, ~10nm of SAM and ~50 nm of gold layer on the top of the wafer.

9. Degree of orientation and Hermans orientation parameter calculations

The degree of orientation and the Hermans orientation parameter were determined by analyzing the azimuthal intensity distribution of the sharp, well-defined (001) diffraction spot, following established analysis protocols.^[25–28] For a simple estimation, the flat component of the azimuthal integration was attributed to an isotropic distribution of crystallites, while the remaining intensity was assigned to preferentially oriented crystallites. This ordering metric does not account for the angular width of the preferential orientations, which can be evaluated from the azimuthal full width at half maximum (FWHM) of the respective peak.

Experimental data were reshaped into 2D diffractograms in reciprocal space using the open-access software GIXSGUI (Figure S15a).^[29] To remove non-sample-related scattering, background contributions from air, the gold substrate, and other sources were estimated by taking azimuthal cuts above and below the peak, averaging them, and subtracting the result from the central cut. For quantitative texture analysis, two corrections were applied to the pole figure data (Figure S15b). First, the signal near 90° (the horizon) was excluded, as it was identified as a Yoneda peak.^[30] Second, the missing wedges at $\chi = 0^\circ$ and 37–54° were accounted for by fitting the remaining data using Gaussian or linear functions, and the full angular range from 0° to 90° was analyzed (Figure S15c).

Correction of the pole figure was performed by multiplying the measured intensity by $\sin(\chi)$. This correction converts the measured scattering intensity around q_z into the total scattering signal that would be expected if all crystallites in the 2D and 3D powder textures were accessible at a given χ . Subsequent normalization of the intensity per area under the diffraction peak enables direct comparison between measurements independent of geometric factors.

The degree of orientation is calculated by

$$DO (\%) = \frac{A_{total} - A_{isotropic}}{A_{total}} \cdot 100$$

where A_{total} is the area below the integrated intensity as a function of azimuthal angle χ , and $A_{isotropic}$ is the isotropic fraction as shown in Figure S15d.

Hermans orientation parameter (HOP) is calculated by the formulas

$$\langle \cos^2 \chi \rangle = \frac{\sum I(\chi) \cos^2 \chi}{\sum I(\chi)}$$

$$HOP = \frac{3\langle \cos^2 \chi \rangle - 1}{2}$$

where $I(\chi)$ is intensity at azimuthal angle χ .

HOP ranges from -0.5 (perfectly perpendicular alignment) to 1 (perfectly aligned along the reference axis) and 0 is fully isotropic distribution.

Although obtaining a complete pole figure down to $\gamma = 0^\circ$ is not possible for reflections along q_z and corrections were therefore applied, the presented methodology provides a few-step approach for GIWAXS data analysis that enables reliable comparison of different datasets and assessment of synthesis reproducibility.

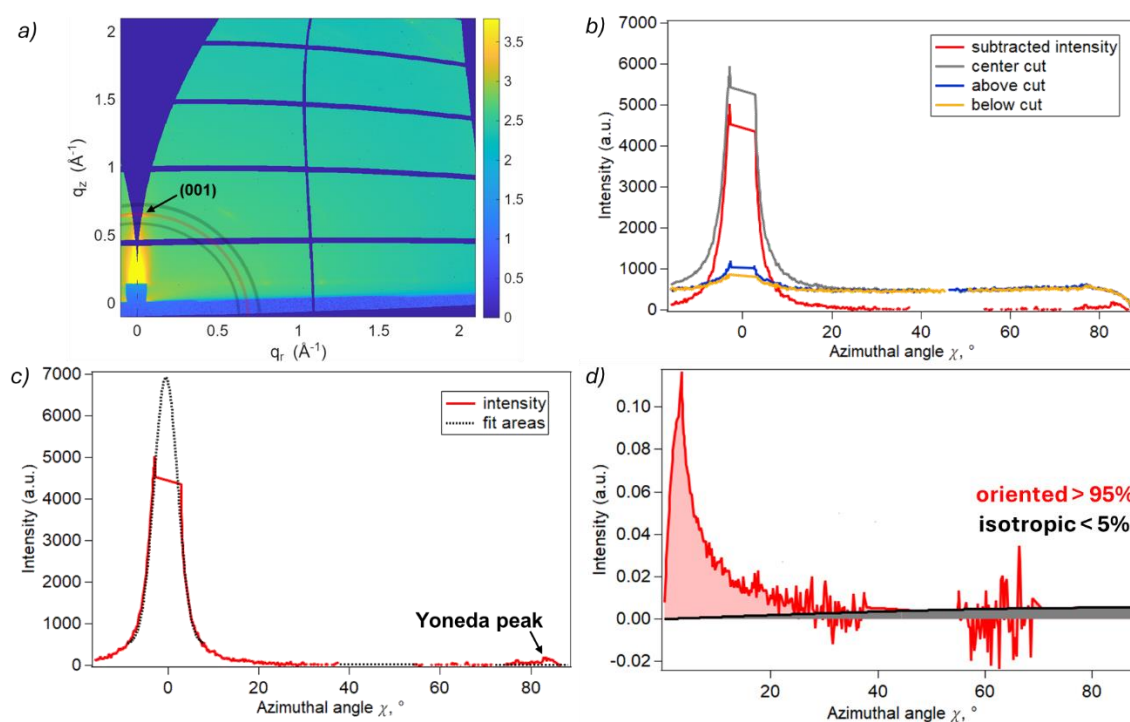


Figure S15. GIWAXS data processing. (a) Reshaped GIWAXS image showing the intense (001) reflection and corresponding azimuthal cuts. (b) Background intensity subtraction. (c) Illustration of corrections applied to the pole figure data, including missing wedge adjustments and geometric weighting. (d) Corrected and area-normalized pole figure intensities highlighting the isotropic crystallite contribution.

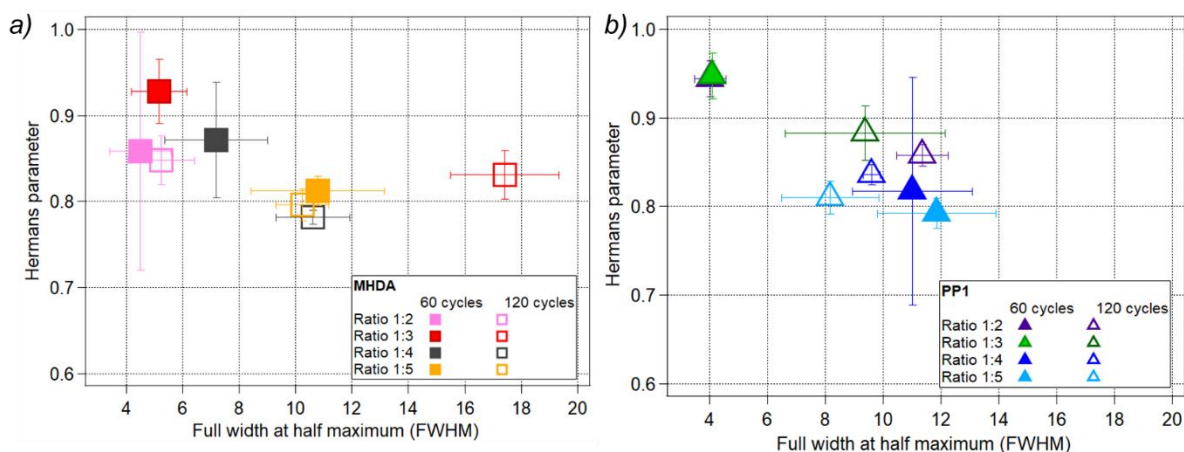


Figure S16. HOP versus azimuthal full width at half maximum (FWHM) for MHDA (a) and PP1 (b) synthesised compounds. The plot illustrates the higher degree of orientation (HOP > 0.85) for samples with BDC:DABCO molar ratios of 1:2 and 1:3 after 60 deposition cycles, consistent with the observed SEM data (Figure 2).

Table 4. The mean values of the DO, HOP and FWHM for samples with different linker-to-linker ratio.

Ratio	SAM	Cycles	DO	HOP	FWHM
1:2	MHDA	60 cycles	68.18 ± 21.19%	0.86 ± 0.14	4.49 ± 1.08
		120 cycles	81.69 ± 5.94%	0.85 ± 0.03	5.23 ± 1.19
	PP1	60 cycles	61.58 ± 18.42%	0.94 ± 0.02	4.04 ± 0.54
		120 cycles	90.27 ± 0.28%	0.86 ± 0.01	11.36 ± 0.87
1:3	MHDA	60 cycles	88.64 ± 7.94%	0.93 ± 0.04	5.18 ± 0.98
		120 cycles	89.64 ± 2.64%	0.83 ± 0.03	17.42 ± 1.93
	PP1	60 cycles	61.30 ± 23.70%	0.95 ± 0.03	4.05 ± 0.27
		120 cycles	90.77 ± 5.59%	0.88 ± 0.03	9.39 ± 2.75
1:4	MHDA	60 cycles	83.33 ± 9.23%	0.87 ± 0.07	7.20 ± 1.83
		120 cycles	87.51 ± 3.50%	0.78 ± 0.01	10.61 ± 1.31
	PP1	60 cycles	88.69 ± 16.91%	0.82 ± 0.13	11.02 ± 2.08
		120 cycles	92.63 ± 3.06%	0.84 ± 0.01	9.62 ± 0.28
1:5	MHDA	60 cycles	83.77 ± 0.20%	0.81 ± 0.01	10.79 ± 2.36
		120 cycles	87.91 ± 0.07%	0.80 ± 0.01	10.24 ± 0.92
	PP1	60 cycles	78.19 ± 2.79%	0.79 ± 0.01	8.18 ± 1.67
		120 cycles	70.40 ± 32.84%	0.81 ± 0.02	9.62 ± 0.28

References

- (1) Burian, M.; Meisenbichler, C.; Naumenko, D.; Amenitsch, H. SAXSDOG : Open Software for Real-Time Azimuthal Integration of 2D Scattering Images. *J Appl Crystallogr* **2022**, *55* (3), 677–685. <https://doi.org/10.1107/S1600576722003685>.
- (2) Dybtsev, D. N.; Chun, H.; Kim, K. Rigid and Flexible: A Highly Porous Metal–Organic Framework with Unusual Guest-Dependent Dynamic Behavior. *Angew Chem Int Ed* **2004**, *43* (38), 5033–5036. <https://doi.org/10.1002/anie.200460712>.
- (3) Singh, M.; Kaur, N.; Comini, E. The Role of Self-Assembled Monolayers in Electronic Devices. *J. Mater. Chem. C* **2020**, *8* (12), 3938–3955. <https://doi.org/10.1039/D0TC00388C>.
- (4) Griffiths, K.; Halcovitch, N. R.; Griffin, J. M. Long-Term Solar Energy Storage under Ambient Conditions in a MOF-Based Solid–Solid Phase-Change Material. *Chem. Mater.* **2020**, *32* (23), 9925–9936. <https://doi.org/10.1021/acs.chemmater.0c02708>.
- (5) Hjorth Larsen, A.; Jørgen Mortensen, J.; Blomqvist, J.; Castelli, I. E.; Christensen, R.; Dulak, M.; Friis, J.; Groves, M. N.; Hammer, B.; Hargus, C.; Hermes, E. D.; Jennings, P. C.; Bjerre Jensen, P.; Kermode, J.; Kitchin, J. R.; Leonhard Kolsbjerg, E.; Kubal, J.; Kaasbjerg, K.; Lysgaard, S.; Bergmann Maronsson, J.; Maxson, T.; Olsen, T.; Pastewka, L.; Peterson, A.; Rostgaard, C.; Schiøtz, J.; Schütt, O.; Strange, M.; Thygesen, K. S.; Vegge, T.; Vilhelmsen, L.; Walter, M.; Zeng, Z.; Jacobsen, K. W. The Atomic Simulation Environment—a Python Library for Working with Atoms. *J. Phys.: Condens. Matter* **2017**, *29* (27), 273002. <https://doi.org/10.1088/1361-648X/aa680e>.
- (6) Blum, V.; Gehrke, R.; Hanke, F.; Havu, P.; Havu, V.; Ren, X.; Reuter, K.; Scheffler, M. Ab Initio Molecular Simulations with Numeric Atom-Centered Orbitals. *Computer Physics Communications* **2009**, *180* (11), 2175–2196. <https://doi.org/10.1016/j.cpc.2009.06.022>.
- (7) Knuth, F.; Carbogno, C.; Atalla, V.; Blum, V.; Scheffler, M. All-Electron Formalism for Total Energy Strain Derivatives and Stress Tensor Components for Numeric Atom-Centered Orbitals. *Computer Physics Communications* **2015**, *190*, 33–50. <https://doi.org/10.1016/j.cpc.2015.01.003>.
- (8) Ren, X.; Rinke, P.; Blum, V.; Wieferink, J.; Tkatchenko, A.; Sanfilippo, A.; Reuter, K.; Scheffler, M. Resolution-of-Identity Approach to Hartree–Fock, Hybrid Density Functionals, RPA, MP2 and GW with Numeric Atom-Centered Orbital Basis

- Functions. *New J. Phys.* **2012**, *14* (5), 053020. <https://doi.org/10.1088/1367-2630/14/5/053020>.
- (9) Yu, V. W.; Corsetti, F.; García, A.; Huhn, W. P.; Jacquelin, M.; Jia, W.; Lange, B.; Lin, L.; Lu, J.; Mi, W.; Seifitokaldani, A.; Vázquez-Mayagoitia, Á.; Yang, C.; Yang, H.; Blum, V. ELSI: A Unified Software Interface for Kohn–Sham Electronic Structure Solvers. *Computer Physics Communications* **2018**, *222*, 267–285. <https://doi.org/10.1016/j.cpc.2017.09.007>.
- (10) Havu, V.; Blum, V.; Havu, P.; Scheffler, M. Efficient Integration for All-Electron Electronic Structure Calculation Using Numeric Basis Functions. *Journal of Computational Physics* **2009**, *228* (22), 8367–8379. <https://doi.org/10.1016/j.jcp.2009.08.008>.
- (11) Ihrig, A. C.; Wieferink, J.; Zhang, I. Y.; Ropo, M.; Ren, X.; Rinke, P.; Scheffler, M.; Blum, V. Accurate Localized Resolution of Identity Approach for Linear-Scaling Hybrid Density Functionals and for Many-Body Perturbation Theory. *New J. Phys.* **2015**, *17* (9), 093020. <https://doi.org/10.1088/1367-2630/17/9/093020>.
- (12) Perdew, J. P.; Burke, K.; Ernzerhof, M. Generalized Gradient Approximation Made Simple. *Phys. Rev. Lett.* **1996**, *77* (18), 3865–3868. <https://doi.org/10.1103/PhysRevLett.77.3865>.
- (13) Tkatchenko, A.; DiStasio, R. A.; Car, R.; Scheffler, M. Accurate and Efficient Method for Many-Body van Der Waals Interactions. *Phys. Rev. Lett.* **2012**, *108* (23), 236402. <https://doi.org/10.1103/PhysRevLett.108.236402>.
- (14) Ambrosetti, A.; Reilly, A. M.; DiStasio, R. A.; Tkatchenko, A. Long-Range Correlation Energy Calculated from Coupled Atomic Response Functions. *The Journal of Chemical Physics* **2014**, *140* (18), 18A508. <https://doi.org/10.1063/1.4865104>.
- (15) Togo, A. First-Principles Phonon Calculations with Phonopy and Phono3py. *J. Phys. Soc. Jpn.* **2023**, *92* (1), 012001. <https://doi.org/10.7566/JPSJ.92.012001>.
- (16) Togo, A.; Chaput, L.; Tadano, T.; Tanaka, I. Implementation Strategies in Phonopy and Phono3py. *J. Phys.: Condens. Matter* **2023**, *35* (35), 353001. <https://doi.org/10.1088/1361-648X/acd831>.
- (17) Skelton, J. M.; Burton, L. A.; Jackson, A. J.; Oba, F.; Parker, S. C.; Walsh, A. Lattice Dynamics of the Tin Sulphides SnS₂, SnS and Sn₂S₃: Vibrational Spectra and Thermal Transport. *Phys. Chem. Chem. Phys.* **2017**, *19* (19), 12452–12465. <https://doi.org/10.1039/C7CP01680H>.

- (18) Skelton-Group/Phonopy-Spectroscopy, 2026. <https://github.com/skelton-group/Phonopy-Spectroscopy> (accessed 2026-01-16).
- (19) *Jmol: an open-source Java viewer for chemical structures in 3D*. <https://jmol.sourceforge.net/> (accessed 2026-01-16).
- (20) Tang, Y.; Dubbeldam, D.; Tanase, S. Water–Ethanol and Methanol–Ethanol Separations Using in Situ Confined Polymer Chains in a Metal–Organic Framework. *ACS Appl. Mater. Interfaces* **2019**, *11* (44), 41383–41393. <https://doi.org/10.1021/acsami.9b14367>.
- (21) Kovalenko, V. I.; Akhmadiyarov, A. A.; Vandyukov, A. E.; Khamatgalimov, A. R. Experimental Vibrational Spectra and Computational Study of 1,4-Diazabicyclo[2.2.2]Octane. *Journal of Molecular Structure* **2012**, *1028*, 134–140. <https://doi.org/10.1016/j.molstruc.2012.06.045>.
- (22) Lugier, O.; Pokharel, U.; Castellanos, S. Impact of Synthetic Conditions on the Morphology and Crystallinity of FDMOF-1(Cu) Thin Films. *Crystal Growth & Design* **2020**, *20* (8), 5302–5309. <https://doi.org/10.1021/acs.cgd.0c00529>.
- (23) Baumgartner, B.; Ikigaki, K.; Okada, K.; Takahashi, M. Infrared Crystallography for Framework and Linker Orientation in Metal–Organic Framework Films. *Chem. Sci.* **2021**, *12* (27), 9298–9308. <https://doi.org/10.1039/D1SC02370E>.
- (24) Henschel, H.; Andersson, A. T.; Jespers, W.; Mehdi Ghahremanpour, M.; Van Der Spoel, D. Theoretical Infrared Spectra: Quantitative Similarity Measures and Force Fields. *J. Chem. Theory Comput.* **2020**, *16* (5), 3307–3315. <https://doi.org/10.1021/acs.jctc.0c00126>.
- (25) Fischer, J. C.; Li, C.; Hamer, S.; Heinke, L.; Herges, R.; Richards, B. S.; Howard, I. A. GIWAXS Characterization of Metal–Organic Framework Thin Films and Heterostructures: Quantifying Structure and Orientation. *Adv Materials Inter* **2023**, *10* (11), 2202259. <https://doi.org/10.1002/admi.202202259>.
- (26) Oesinghaus, L.; Schlipf, J.; Giesbrecht, N.; Song, L.; Hu, Y.; Bein, T.; Docampo, P.; Müller-Buschbaum, P. Toward Tailored Film Morphologies: The Origin of Crystal Orientation in Hybrid Perovskite Thin Films. *Adv Materials Inter* **2016**, *3* (19), 1600403. <https://doi.org/10.1002/admi.201600403>.
- (27) Gasser, F.; Simbrunner, J.; Huck, M.; Moser, A.; Steinrück, H.-G.; Resel, R. Intensity Corrections for Grazing-Incidence X-Ray Diffraction of Thin Films Using Static Area Detectors. *J Appl Crystallogr* **2025**, *58* (1), 96–106. <https://doi.org/10.1107/S1600576724010628>.

- (28) Klokic, S.; Naumenko, D.; Marmiroli, B.; Carraro, F.; Linares-Moreau, M.; Zilio, S. D.; Birarda, G.; Kargl, R.; Falcaro, P.; Amenitsch, H. Unraveling the Timescale of the Structural Photo-Response within Oriented Metal–Organic Framework Films. *Chem. Sci.* **2022**, *13* (40), 11869–11877. <https://doi.org/10.1039/D2SC02405E>.
- (29) Jiang, Z. *GIXSGUI*: A MATLAB Toolbox for Grazing-Incidence X-Ray Scattering Data Visualization and Reduction, and Indexing of Buried Three-Dimensional Periodic Nanostructured Films. *J Appl Crystallogr* **2015**, *48* (3), 917–926. <https://doi.org/10.1107/S1600576715004434>.
- (30) Yoneda, Y. Anomalous Surface Reflection of X Rays. *Phys. Rev.* **1963**, *131* (5), 2010–2013. <https://doi.org/10.1103/PhysRev.131.2010>.